WEATHERING INTENSITY AND LITHIUM ISOTOPES: A REACTIVE TRANSPORT PERSPECTIVE

Matthew J. Winnick[1*], Jennifer L. Druhan[2], Kate Maher[3]

[1] Department of Geosciences
University of Massachusetts Amherst
Amherst, MA 01003, USA

[2] Department of Geology
University of Illinois Urbana Champaign,
Urbana, IL

[3] Department of Earth System Science
Stanford University
Stanford, CA 94305, USA

[*] Corresponding Author:
mwinnick@umass.edu
627 N Pleasant St,
Morrill II Rm 233, Geosciences
Amherst, MA 01003, USA

This manuscript has been submitted for publication in the American Journal of Science. This version has undergone one round of peer review; however, this manuscript has not yet been accepted for publication. Future versions of this manuscript may have altered content addressing subsequent revisions in response to peer review. If accepted the final version of this manuscript will be available via the DOI link on the right-hand side of this webpage. Please contact the authors with any feedback.

ABSTRACT. Lithium isotopes have emerged as a powerful tool to probe the response of global weathering to changes in climate. Due to the preferential incorporation of ^{6}Li into clay minerals during chemical weathering, the isotope ratio δ^7Li may be used to interrogate the balance of primary mineral dissolution and clay precipitation. This balance has been linked to relative rates of chemical and physical denudation, such that dissolved δ^7Li (δ^7Li_{diss}) is highest at moderate weathering intensities when chemical and physical denudation are comparable. However, we argue that current theory linking δ^7Li to weathering regimes through fluid travel times are unable to explain observations of low δ^7Li and high Li concentrations in rapidly eroding settings. In this study, we re-examine the relationships between δ^7Li, Li concentration, and weathering regime by incorporating Li isotopes into simulations of weathering profiles using a reactive transport model (CrunchFlow) that includes advective fluxes of regolith to simulate variable erosion rates in response to uplift. In these simulations, fractionation is implemented through a kinetic fractionation factor during clay precipitation, which allows the δ^7Li of dissolved and suspended loads in the model to vary as a function of Li/Al ratios in primary and secondary minerals. When the model is run over a range of infiltration and erosion rates, simulations reproduce observed global patterns of δ^7Li_{diss} and suspended load δ^7Li as a function of weathering intensity, controlled primarily by water travel times and mineral residence times in weathered bedrock. We find that reduced water travel times at low weathering intensity, however, are inconsistent with observations of high Li concentrations. As an alternative, we demonstrate how the rapid weathering of soluble, Li-rich minerals such as chlorite under low weathering intensities may resolve this apparent discrepancy between data and theory. We also suggest that observed patterns are consistent with geothermal Li sources under low weathering intensities. This work offers a foundation guiding future studies in testing potential mechanisms underlying global riverine δ^7Li_{diss}.

INTRODUCTION

Chemical weathering, comprising the dissolution of carbonate and silicate minerals along with the oxidation of sulfides and petrogenic carbon, is thought to be a primary regulator of atmospheric composition on geologic timescales. The connections between chemical weathering

and climate are therefore central to our understanding of the evolution of global biogeochemical cycles through Earth history. Over the past two decades, lithium isotopes have emerged as a powerful tool for characterizing the relationships between silicate weathering and past climates. Proxy records of oceanic δ^7Li have been used, for example, to characterize connections between weathering and Cenozoic cooling (Misra and Froelich, 2012; Li and West, 2014; Caves-Rugenstien and others, 2019; Pogge von Strandmann and others, 2020), along with the response of weathering to major carbon cycle perturbations including Ocean Anoxic Events (OAE's) 1 and 2 (Pogge von Strandmann and others, 2013; Lechler and others, 2015), the Permian-Triassic boundary (Sun and others, 2018), and global glaciation events (Pogge von Strandmann and others, 2017). Interpretations of these proxy records rely on modern observations of lithium isotopes in weathering environments; however, even present-day connections between δ^7Li and weathering dynamics have proven highly complex.

The use of lithium isotopes to probe weathering dynamics is enabled by the fact that the lighter isotope, ^{6}Li, is preferentially incorporated into secondary minerals relative to the heavy isotope, ^{7}Li, during the chemical weathering of primary minerals in bedrock. Here, δ^7Li is defined in standard delta-notation as,

$$\delta^7 Li = \left(\frac{^7Li/^6Li_{sample}}{^7Li/^6Li_{L-SVEC}} - 1\right) * 1000‰ \qquad (1),$$

where $(^7Li/^6Li)_{L\text{-}SVEC}$ is the isotope ratio of the L-SVEC standard, 12.2998 (Flesch and others, 1973).

Isotope fractionation during secondary mineral precipitation represents a combination of effects relating to the incorporation of Li into mineral structural sites (Williams and Hervig, 2005; Vigier and others, 2008; Wimpenny and others, 2010) and inner-sphere sorption (Zhang and others, 1998; Anghel and others, 2002; Pistiner and Henderson, 2003; Hindshaw and others, 2019) as potentially modified by OH group abundance (Millot and Girard, 2007). Secondary mineral phase δ^7Li values are thus offset from primary minerals by -5‰ to -30‰, reflecting this preferential uptake of ^{6}Li (Vigier and others, 2008; Chan and others, 1992; Williams and Hervig, 2005). As a result, global riverine δ^7Li_{diss} values (-2 to >30‰) are significantly enriched relative to average upper continental crust materials (-2-6‰) (Tomascak, 2004; Pogge von Strandmann and others, 2020).

When solutes are enriched in ^{7}Li relative to bedrock, the dissolved δ^7Li (δ^7Li_{diss}) reflects the balance between Li release from primary mineral dissolution and Li incorporation into secondary minerals. During congruent weathering, the Li released from primary minerals remains in solution and δ^7Li_{diss} resembles bedrock values; when weathering is incongruent and a significant amount of Li is incorporated into secondary minerals, δ^7Li_{diss} is elevated relative to the minerals. Accordingly, observations of modern river systems show that δ^7Li_{diss} varies as a function of weathering congruency, or the fraction of Li released from primary mineral dissolution that remains in solution and is not incorporated into secondary minerals (f_{Li}) (Dellinger and others, 2015). Notably, the overall pattern of this relationship segregates into two unique relationships, one in upland environments where the degree of δ^7Li_{diss} elevation above bedrock values varies as a linear function f_{Li}, and the second in floodplain environments where δ^7Li_{diss} varies as a power-law or Rayleigh-style function of f_{Li} potentially due to scavenging of Li by extant phases (Dellinger and others, 2015; Maffre and others, 2020) or the formation of authigenic clays (Zhang and others, 2021). Here, we focus on Li fractionation processes characteristic of upland regolith development.

Extending the relationship between δ^7Li and weathering congruence to a metric for weathering fluxes has proven more difficult. For example, δ^7Li_{diss} has been empirically linked to both chemical weathering fluxes and riverine Li concentrations within specific regions; however, these relationships may be contradictory in both sign and magnitude when compared across regions (Huh and others, 2001; Vigier and others, 2009; Millot and others, 2010). More recent work, both theoretical and observational (Bouchez and others, 2013; Dellinger and others, 2015, 2017), has contended that δ^7Li_{diss} reflects weathering intensity (WI), or the ratio of chemical weathering (W) to total denudation, D (~E + W). At steady state regolith thickness, regolith production (RP) must equal total denudation (RP = E + W), hence we define WI = W/RP, as outlined in figure 1. Within this framework, weathering congruence and subsequent δ^7Li_{diss} are controlled by weathering intensity, which in turn dictates the combination of mineral residence- and fluid travel times in the regolith.

In figure 1, Point A represents a condition of moderate WI where physical and chemical erosion are comparable. Under these conditions, regolith profiles reflect the balance between regolith production and denudation rates, as minerals are supplied via uplift and are partially depleted towards the surface through chemical denudation before they are eroded. As a result of

these well-developed regolith profiles, fluid travel times during infiltration are sufficient to support secondary mineral precipitation, mineral residence times are sufficient to support secondary mineral accumulation, and weathering occurs incongruently. This situation results in maximum δ^7Li_{diss} values and moderate Li concentrations ($[Li^+]$; $\sim10^2$ nM; Dellinger and others, 2015). When chemical denudation rates are much greater than erosion or regolith production (high WI, Point B), chemical weathering depletes primary minerals from soils (i.e. supply-limited weathering), and dissolved solutes represent the dissolution of low-solubility secondary mineral phases, characteristic of wet tropical environments (von Blanckenburg and others, 2004). Due to this low solubility and the preferential uptake of ^6Li during initial clay precipitation, clay dissolution results in both low $[Li^+]$ (<10 nM) and low δ^7Li_{diss}.

Finally, under low WI conditions when physical erosion greatly outpaces chemical weathering (Point C), mineral residence times in regolith are short such that secondary minerals are unable to accumulate in significant amounts (i.e. kinetic-limited weathering). Steady-state weathering models that describe this behavior predict that under low WI, clay precipitation rates are reduced relative to primary mineral dissolution rates (Chamberlain and others, 2005; Ferrier and Kirchner, 2008), resulting in congruent weathering and low, bedrock-like δ^7Li_{diss} values (Bouchez and others, 2013). This conceptual model of congruent weathering under low WI implicitly encapsulates fluid travel times (via their dissolution/precipitation rate parameterizations), suggesting that infiltration rates are too short to support active clay precipitation, possibly due to thin soil mantles. Examples of fluid travel time controls on the extent of δ^7Li_{diss} have also been demonstrated by previous reactive transport studies (Wanner and others, 2014; Bohlin and Bickle, 2019; Golla et al. 2021). We note, however, that observations of low clay content in low WI environments may arise from reduced timescales for accumulation due to short regolith residence times, rather than slow clay precipitation rates. Here, we show that fluid travel time controls lead to a notable discrepancy between theories that predict low $[Li^+]$ at low WI due to short fluid travel times, and observations that show the highest $[Li^+]$ in low WI systems. To our knowledge, this discrepancy has not previously been articulated.

Specifically, observations of $[Li^+]$ in global rivers show the highest concentrations on the order of $>10^3$ nM in low WI and rapidly eroding environments (Dellinger and others, 2015; Pogge von Strandmann and Henderson, 2015), leading to a parabolic relationship between δ^7Li_{diss} and $[Li^+]$, similar to that of δ^7Li_{diss} and WI (fig. 1). However, short fluid travel times and

reduced clay precipitation should theoretically limit overall primary mineral dissolution and the subsequent accumulation of Li in solution, as balanced by reduced clay Li uptake. In fact, some field sites do show the co-limitation of clay precipitation and associated primary mineral dissolution under short fluid travel times, wherein high river discharge results in diluted [Li^+] and low δ^7Li_{diss} values relative to baseflow (Lemarchand and others, 2010; Manaka and others, 2017).

Herein, we explore this apparent paradox and the links between weathering intensity and congruence using a reactive transport model of lithium isotopes. Through the incorporation of lithium isotope dynamics into the CrunchFlow reactive transport code (Steefel and others 2015), we expand on previous observational and theoretical formulations through the contemporaneous representation of fluid flow (Maher 2010), multi-component mineral dissolution and precipitation reactions (Steefel and others, 2015), erosional forcing (Maher and Chamberlain, 2014), and isotope fractionation (Druhan and others, 2013; Wanner and others, 2014; Maher and von Blanckenburg, 2016; Golla et al. 2021). Simulations across a range of weathering intensity scenarios are evaluated against observations of riverine δ^7Li_{diss}, making use of an update to the CrunchFlow software facilitating fractionating precipitation and non-fractionating dissolution of a given mineral phase. We also explore the transient evolution of weathering profiles under varying weathering intensities, along with the potential role for changes in weathering zone mineralogy to influence observed lithium isotope dynamics. While we acknowledge the broad and seminal applications of δ^7Li to study weathering processes across the globe in many other studies, we restrict our data-model comparison to data presented in Dellinger and others (2014, 2015, 2017) based on their framework for interpreting δ^7Li signals as a function of Li/Al ratios. This normalization allows comparison across a diversity of bedrock types.

METHODS

Mineralogy and Geochemistry

In order to probe the relationships between weathering intensity, congruence, and δ^7Li, we simulated upland weathering profiles using the reactive transport software CrunchFlow, making use of the isotope features developed in prior studies and a software update necessary to

treat isotopes in systems of high weathering intensity. In CrunchFlow, mineral dissolution/precipitation rates are represented by Transition State Theory (TST)-style rate laws (cf. Lasaga, 1998) with a dependence on reaction affinity that allows dissolution/precipitation to occur only when solutes are under/over-saturated with respect to that given mineral phase, as

$$R_{net} = k_d * SA * \left(\frac{Q}{K_{eq}} - 1\right) \qquad (2),$$

where R_{net} is the net reaction rate for a specified mineral, k_d is a temperature-dependent intrinsic rate constant, SA is mineral surface area, Q is the ion activity product, and K_{eq} is the mineral equilibrium constant, and the ($Q/K_{eq} - 1$) term represents reaction affinity. The composition of each solid phase is described as a stoichiometric and charge balanced assemblage of primary species, thus assuring mass balance between co-evolving dissolved solutes and solids.

One important effect of this affinity dependence is that it directly links the rate of primary mineral dissolution to the rate of secondary mineral precipitation. A common example is the precipitation of Al and Si to form secondary phases, which maintains undersaturated solute concentrations with respect to primary minerals bearing these elements (Zhu and others, 2005; Maher and others, 2006). Hence, the removal of weathering products into clay minerals allows mineral dissolution to continue by increasing the driving force for dissolution via the reaction affinity. This affinity dependence is not included in the regolith models that have primarily informed theoretical considerations of Li isotopes in previous studies (Chamberlain and others, 2005; Ferrier and Kirchner, 2008; Bouchez and others, 2013). In these models, variation in primary mineral dissolution occurs independent of clay precipitation, where the latter is parameterized as a constant rate. We note that these models were originally developed to track the evolution of solid-phase weathering zone mineralogy (Chamberlain and others, 2005; Ferrier and Kirchner, 2008). However, dissolved Li isotope compositions in these models are controlled by the relative kinetic rates of primary mineral dissolution and clay precipitation and are thus uniquely sensitive to rate parameterizations (Bouchez and others, 2013). More recently, a CrunchFlow model was developed for Li isotope fractionation associated with an upland shale weathering profile (Golla et al. 2021). This study demonstrated the functionality of explicit

coupling between primary mineral dissolution and secondary mineral precipitation and successfully reproduced fluid δ^7Li profiles through the bedrock vadose zone and groundwater.

Here we generalize the approach taken in Golla et al. (2021) using a representative granitic weathering profile simulated as in Maher (2011), with bedrock modeled as a combination of 60% volume quartz, 30% plagioclase feldspar (20% anorthite, 80% albite), and 2% halloysite, leaving ~8% protolith porosity. Equilibrium constants were used primarily from the EQ3/EQ6 thermodynamic database (Wolery and others, 1990), supplemented with plagioclase equilibrium constants from Arnorsson and Stefansson (1999). Intrinsic rate constants and activation energies were taken from a compilation by Palandri and Kharaka (2004). Mineral reactions, kinetic rate constants (k_d) , and equilibrium constants (K_{eq}) are shown in Table 1, and we note that as in equation (2), affinity dependence is assumed to be linear for simplicity.

Additional simulations were conducted including a high solubility chlorite mineral at 7.5% volume with quartz reduced to 52.5% to maintain porosity. We include these simulations as Li is often preferentially concentrated in ferro-magnesian minerals, substituting for Mg^{2+} and Fe^{2+} due to similar ionic radii (Tardy and others, 1972; Penniston-Dorland and others, 2017). We use the reaction stoichiometry and equilibrium constants for chlorite and intermediate weathering product vermiculite from Heidari and others (2017) based on constrained reactive transport simulations of weathering in the Shale Hills Critical Zone Observatory. We amend mineral stoichiometry such that Li^+ substitutes for Fe^{2+}. Additionally, we assume no fractionation during vermiculitization by enforcing the same ^{7}Li:^{6}Li ratios in chlorite and vermiculite. We note that the choice of chlorite rather than other Li-rich soluble minerals such as lithium-bearing alkali amphiboles is primarily based on the existence well-established CrunchFlow reaction networks constrained by field studies (Heidari and others, 2017). However, the relationship between chlorite lithium dynamics and weathering intensity investigated here are theoretically transferrable to other highly soluble, lithium-rich minerals.

Lithium Isotope Parameterizations

Lithium isotopes were incorporated into these simulations by defining ^{6}Li and ^{7}Li as separate primary chemical species. To capture typical bedrock compositions, Li was incorporated into plagioclase minerals as a solid solution with Na, which offers a simple means

of maintaining charge balance. The ^{6}Li and ^{7}Li values are set such that $\delta^{7}Li_{bedrock}$ is 0‰ and total concentration in our granitic mineral assemblage is ~40 ppm, within error of average upper continental crust (Teng and others, 2004). The inclusion of Li-rich chlorite in our mineral assemblage raises bedrock Li concentrations to ~60 ppm, more characteristic of shale concentrations (Holland, 1984) and bedrock within the low WI watersheds of the Beni river (Dellinger and others, 2015). Based on observations of stoichiometric dissolution of ^{6}Li and ^{7}Li from primary silicate minerals, we assume no fractionation during dissolution, and ^{6}Li and ^{7}Li are incorporated into a single mineral with a single K_{eq} and k_d value as shown in Table 1.

To simulate fractionation during clay precipitation, we employ a solid-solution approach that consists of two isotopic end-member phases: ^{6}Li-Halloysite and ^{7}Li-Halloysite (Druhan and others, 2013). The coupled rate expressions for precipitation of these phases are,

$$R_{6Li-H} = \frac{[^{6}Li^{+}]}{[^{6}Li^{+} + {}^{7}Li^{+}]} * k_{6Li-H} * SA_H * \left(\frac{Q_{cc}}{K_{eq}} - 1\right), \quad (3) \qquad \text{and}$$

$$R_{7Li-H} = \frac{[^{7}Li^{+}]}{[^{6}Li^{+}]} * \frac{[^{6}Li^{+}]}{[^{6}Li^{+} + {}^{7}Li^{+}]} * \alpha_k * k_{6Li-H} * SA_H * \left(\frac{Q_{cc}}{K_{eq}} - 1\right), \quad (4)$$

where Q_{cc} is the total ion activity product (including ^{6}Li and ^{7}Li) with respect to the combined halloysite phases, K_{eq} is the equilibrium constant (same for both phases), and α_k is the kinetic fractionation factor ($k_{7Li\text{-}H}/k_{6Li\text{-}H}$) after Druhan and others (2013) and Steefel and others (2014). As described in Steefel and others (2014), this formulation assumes that the isotopic composition of the solid phase does not play a role in fractionation during precipitation through the mineral isotopologue activities. Fractionation occurs solely as a result of specified differences in intrinsic rate constants between isotopologue clay phases. Thus, under appropriately simplified conditions, this model would create Rayleigh distillation-style fractionation in the $\delta^{7}Li_{diss}$ as $[Li^{+}]$ is lost from solution due to clay precipitation. In other words, removal of Li from solution due to clay precipitation in the absence of primary mineral Li inputs would act as an open-system process with a constant fractionation at far-from-equilibrium conditions, similar to Rayleigh distillation.

In our simulations, we assume a kinetic fractionation factor of $\alpha_k = 0.982$ for precipitation of the halloysite solid solution. This value is based on calculated fractionation

283 factors from upland environments in the Dellinger and others (2015) dataset and falls roughly in
284 line with experimental values (Vigier and others, 2008). As in previous modeling studies, this
285 fractionation is meant to encompass a range of potential processes including structural
286 substitution, interlayer exchange, and surface sorption (Bouchez and others, 2013; Wanner and
287 others, 2014). Notably, in our treatment, Li uptake by clay is simulated via charge balance with
288 Al (Table 1), which is necessary within CrunchFlow. Rather than the direct structural
289 substitution of Li for Al, this parameterization is meant to reflect effective Li uptake by clays
290 that includes mechanisms such as sorption, interlayer exchange, and structural substitution.
291 The magnitude of observed fractionation in solutes is also controlled by the partition
292 coefficient for Li into clays, which reflects the ratio of lithium dissolved from primary minerals
293 that is incorporated into clays (P_{Li}) versus left in solution (f_{Li}) at equilibrium. Under this
294 formulation, $P_{Li} = (1- f_{Li})$. The result is that isotopic signals in the dissolved phase are maximized
295 when almost all the lithium released via dissolution is incorporated into secondary precipitates.
296 To examine the sensitivity of fractionation to P_{Li}, we manually vary the concentration of clay Li
297 such that P_{Li} ranges from 0.01 to 0.99 (x values in Table 1). Under this formulation, P_{Li} is equal
298 to the ratio of Li/Al in Halloysite to Plag(An_{20}) (i.e. $P_{Li} = (x/2)/(0.0026/1.2)$). This range of P_{Li}
299 values is based on field observations of f_{Li} across South American watersheds, calculated from
300 ratios of Li/Al in suspended sediments to bedrock (Dellinger et al., 2015).
301 We chose to simulate a simple 1:1 clay phase (halloysite) rather than a suite of competing
302 clay phases including more complex 2:1 clays in order to maintain constant P_{Li} values within a
303 given model run. This reasoning also underlies our choice to represent an 'effective' clay uptake
304 rather than explicit representations of sorption, interlayer exchanges, and structural substitution.
305 Under these more complex representations, P_{Li} would necessarily vary within an individual
306 model run through time and with depth as the weathering reaction network evolved or Li actively
307 exchanged with clay phases. While these dynamics certainly impact Li during weathering, they
308 have not been adequately linked to mineral residence or fluid travel times in natural
309 environments, which are the primary focus of our analyses. Thus, any encapsulated links
310 between P_{Li} and erosion and flow rates would not be justified by previous literature. Our
311 simplified representation allows us to isolate the impacts of erosion and flow rates across a range
312 of set P_{Li} values and facilitates the direct comparison to Dellinger and others (2015, 2017)
313 observations. As described above, these are based on Li/Al ratios in bedrock versus dissolved

and suspended loads and thus also represent a composite suite of 'effective' uptake mechanisms. We note that *x* is the same within any given simulation for ^{6}Li-Halloysite and ^{7}Li-Halloysite such that fractionation is only induced by the kinetic fractionation factor. For simplicity, we assume that Li substitution at ppm levels does not impact K_{eq} values (Wang and Xu, 2001).

Software Update for Isotope Partitioning at High Weathering Intensity

As discussed above, the high weathering intensity regime requires that isotopically distinct secondary clays are ultimately re-dissolved into the fluid phase. However, equations (3) and (4) are not applicable under conditions where $\frac{Q_{cc}}{K_{eq}} < 1$ for the following reasons. First, the fractionation factor ($\alpha_k = 0.982$) would result in a more rapid reaction rate for the ^{6}Li end-member relative to ^{7}Li during dissolution. This would mean that the ^{6}Li-bearing halloysite (eq. 3) would dissolve faster than its counterpart, leading to spurious fractionation over the timescales considered here. Second, equations (3) and (4) contain no reference to the isotopic composition of the solid phase, and thus there is no ability to incorporate the isotope ratio of the halloysite that is being solubilized into the fluid phase within this framework. To address these issues, we use the version of the isotopic solid solution model originally developed in CrunchFlow (Druhan and others, 2013) where the solid solution ratio is based on the isotopic mole fractions of the mineral phase:

$$R_{6Li-H} = Y_{6Li-H} * k_{6Li-H} * SA_H * \left(\frac{Q_{cc}}{Y_{6Li-H} * K_{eq}} - 1\right), \quad (5) \text{ and}$$

$$R_{7Li-H} = Y_{7Li-H} * \alpha_k * k_{6Li-H} * SA_H * \left(\frac{[^{7}Li^{+}]}{[^{6}Li^{+}]} \frac{Q_{cc}}{Y_{7Li-H} * K_{eq}} - 1\right), \quad (6)$$

Where Y is the isotopic mole fraction or the number of moles of a given isotope of lithium per total number of moles of lithium in the halloysite phase.

To stoichiometrically dissolve halloysite that was originally formed following the coupled rate laws given in equations (3) and (4), we modify the original formulation of equations (5) and (6) such that the kinetic fractionation factor α_k is set to 1.0 (no fractionation) and thus the

two minerals dissolve at the same relative rates. The result is that the isotope ratio of the neo-formed halloysite mineral will be delivered into the fluid phase, ensuring stoichiometric dissolution without spurious fractionation:

$$R_{6Li-H} = \begin{cases} eq.3, & \frac{Q_{cc}}{K_{eq}} \geq 1 \\ eq.5, & \frac{Q_{cc}}{K_{eq}} < 1 \end{cases} \quad \text{(7a) and}$$

$$R_{7Li-H} = \begin{cases} eq.4, \alpha_k = 0.982, & \frac{Q_{cc}}{K_{eq}} \geq 1 \\ eq.6, \alpha_k = 1.000, & \frac{Q_{cc}}{K_{eq}} < 1 \end{cases} \quad \text{(7b)}$$

A similar approach was utilized in Golla et al. (2021) for the development of a weathering profile model incorporating Li isotopes specifically to reproduce a measured dataset of vadose zone and groundwater samples.

Weathering Scenarios

We simulate four separate weathering scenarios, sequentially increasing in complexity, to test the controls of weathering regimes on Li systematics as outlined in Table 2.

- Scenario 1- Batch Reactor: we simulate batch reactor weathering reactions, to evaluate temporal trends in solute concentrations and to analyze the sensitivity of Li fractionation to Li congruence.
- Scenario 2- Chronosequence: we simulate a 1-D weathering profile chronosequence with no uplift/erosion to evaluate temporal trends in mineralogical and solute profiles.
- Scenario 3- Uplift/Erosion: we simulate 1-D weathering profiles with specified regolith production rates to test the controls of weathering intensity.
- Scenario 4- Uplift/Erosion with chlorite: we incorporate soluble, Li-rich chlorite into our 1-D uplift/erosion profiles to test their potential controls on Li systematics.

Model set-up and boundary conditions are described in detail in the following subsections.

Scenario 1 - Batch reactors: To examine the general characteristics of our Li isotope parameterizations, we first simulate a simple batch reactor with no transport. These are initialized with an un-weathered primary mineral composition, dilute waters, a temperature of 15° C, and fixed open-system pCO_2 of 5000 ppm, setting an initial pH of 5.0 that increases with

progressive mineral dissolution/precipitation reactions. This pCO_2 choice is meant to reflect typical elevated values in soil environments due to oxidation of organic matter. We note that increased (decreased) pCO_2 leads to increased (decreased) equilibrium solute concentrations (Winnick and Maher, 2018), but does not influence isotopic evolution. Within these batch simulations, we vary the partition coefficient P_{Li} from 0.01-0.99 via x values as defined in *Lithium Isotope Parameterizations* and shown in Table 1 for the halloysite phase. In each simulation, reaction progress is monitored for 5 kyr. We also demonstrate how the simulation of a 2:1 clay (Ca-beidellite) results in the same lithium fractionation dynamics as a function of P_{Li} as halloysite in Appendix A.

Scenario 2 - Chronosequence: Next, we simulate 1-D weathering profiles with no erosion to characterize the temporal evolution of solid and aqueous geochemical profiles. Weathering domains are set to 10 m with a grid cell size of 5 cm (200 cells). Initial porosity is set to 7%, and weathering occurs under 75% water saturation and a large prescribed gas flux of CO_2 into the domain to maintain open-system weathering conditions (Winnick and Maher, 2018). As in the batch simulations, profiles are initialized with an un-weathered primary mineral composition, dilute waters, a temperature of 15° C, and pCO_2 of 5000 ppm. Water infiltrates through the domain via Darcy flux with a prescribed rate of 0.5 m/yr. Simulations are run for 1 Myr, and changes in solid and aqueous geochemistry are analyzed at multiple timesteps.

Scenario 3 - Uplift/Erosion: We analyze the effects of variable weathering intensity by simulating 1-D weathering profiles with prescribed volumetric uplift/erosional forcing. CrunchFlow incorporates uplift/erosion through the specification of a volumetric uplift rate at the bottom of the domain equivalent to a regolith production rate. Material is removed from the top of the domain at the same volumetric rate; however, mass erosion rates are reduced relative to regolith production due to chemical denudation of material before it is uplifted and removed at the surface (fig. 1). Weathering domains, water saturation, and pCO_2 are set as in chronosequence simulations. To examine the relationship between lithium isotope dynamics and reactive transport, we simulated a suite of weathering regimes by varying infiltration and erosion rates. Infiltration (Darcy flux) was varied between 0.1-5 m/yr, and regolith production (volumetric erosion) was varied between 0.005-0.2 mm/yr, corresponding to erosion rates of 1.4

– 485 t/km^2/yr after correcting for porosity changes during weathering (Table 3), resulting in 30 unique weathering intensity regimes. Each weathering simulation was run for 0.5 Myr, resulting in either the development of a steady-state profile (constant aqueous and solid geochemical depth profiles) or transient profiles (time-dependent geochemical depth profiles characterized by the progressive depletion of primary minerals). Model output was analyzed at multiple timesteps to characterize the temporal evolution of mineral and solute profiles.

We define the regolith weathering zone within each time-step as model cells with >101% initial bedrock porosity. This depth is meant to represent a conservative estimate of the weathering front based on observable changes in bulk density (Maher and von Blanckenburg, 2016). We note that other modeling studies evaluate weathering depths based on solute equilibrium length scales (Lebedeva and others, 2010), which in our simulations always occur below the porosity-based weathering front. Our definition of weathering zone is meant to capture potential contrasts in permeability that may affect subsurface flowpaths and travel times. Specifically, due to the model setup which specifies constant Darcy flow, simulated water fluxes do not vary within the profile domain based on porosity changes. To capture short fluid travel times associated with preferential and interflow caused by thin regolith and sharp permeability contrasts between weathered and fresh bedrock, we evaluate solute concentrations and δ^7Li_{diss} at the base of this regolith weathering zone in addition to the base of the model domain. In the simulations with low regolith production rates that result in weathering of the entire domain, we evaluate solute concentrations at 9 m depth to avoid boundary condition effects associated with the bedrock boundary condition at 10 m.

Model outputs and metric calculations are shown in Table 3. Mass erosion rates are calculated by multiplying the specified regolith production rate by bulk density in the top model cell. Riverine suspended material is taken as the mineralogical composition of the eroding top cell of the domain. Chemical denudation rate is calculated as the sum of major dissolved weathering products ($[Ca^{2+}]+[Mg^{2+}]+[Na^{+}]+[K^{+}]+[SiO_{2(aq)}]$) multiplied by the prescribed infiltration rate at both the domain boundary and at the bottom of the regolith weathering zone. Finally, a metric of weathering incongruence (I) is calculated based on the ratio of the instantaneous rate of halloysite precipitation to plagioclase dissolution ($I = -R_{halloysite}/R_{plagioclase}$; as per equation (2), precipitation is a positive rate, and dissolution is a negative rate. This metric is similar to qualitative descriptions of weathering incongruence under conditions of plagioclase

dissolution and halloysite precipitation, in which incongruence represents the molar ratio of clay formation to primary mineral dissolution. When halloysite dissolves, however, incongruence is calculated as a negative number.

Scenario 4 – Uplift/Erosion with chlorite.— To address the potential role of soluble, Li-rich ferro-magnesian minerals such as chlorite in driving global δ^7Li_{diss} patterns, we conduct a series of simulations including an amended chlorite mineral as shown in Table 1. The weathering of chlorite minerals involves a multi-step reaction series by which, first, cations in the octahedral coordination layer (Mg^{2+}, Fe^{2+}) are leached in a process referred to as supergene 'vermiculitization' (Proust and others, 1986). In general, this weathering step is not well-characterized in field environments due to analytical challenges involved in distinguishing unaltered chlorite and vermiculite. Recent studies, however, have made use of ratios of 7Å to 14 Å XRD peaks along with stoichiometric characterizations to demonstrate vermiculitization in deep regolith profiles (Sullivan and others, 2016; Gu and others, 2020). Following vermiculitization, which may involve intermediate products of interstratified chlorite/vermiculite, vermiculite products are further weathered to kaolinite-type clays.

To represent this multi-step process, we have included an intermediate, lower solubility vermiculite mineral in addition to chlorite following the methodology of Heidari and others (2017) (Table 1). In terms of Li^+, we assume no fractionation during 'vermiculitization' by incorporating equivalent $^7Li^+$:$^6Li^+$ ratios in mineral stoichiometry. Further, we assume that Li^+ leaching relative to Al^{3+} falls intermediately between simulated leaching of Mg^{2+} and Fe^{2+} in order to maintain realistic dissolved Li concentrations ($<10^4$ nM).

In these chlorite simulations, bedrock is initialized as 52.5% quartz, 30% plagioclase (An20), 7.5% 'chlorite' (6% chlorite, 1.5% vermiculite), and 2% halloysite. We note that these mineral constituents are similar to quartz diorite in the Luquillo Critical Zone Observatory (Murphy and others, 1997), whereas weathering fluxes from shale environments are more likely to be dominated by chlorite, other clay minerals, with smaller amounts of plagioclase (Gu and others, 2020). We conduct 1-D uplift/erosion weathering profiles under the same conditions as described above.

RESULTS

Batch Reactor Results (Scenario 1)

At the start of batch reactor simulations (Scenario 1), dilute waters are undersaturated with respect to both plagioclase and halloysite, and primary mineral dissolution and secondary mineral precipitation proceed as solute concentration profiles stabilize over roughly 10^2 years (fig. 2). When the simulation begins, plagioclase dissolution is at its maximum rate, which is sustained for the first ~6 months of simulation, representing kinetic controls. As solute concentrations increase and waters approach saturation, a quasi-steady state develops in the aqueous profiles and the affinity term in equation (2) becomes the limiting factor on dissolution rates, which subsequently approach zero. We note that in these batch reactor scenarios, plagioclase depletion is minimal, such that changes in surface area do not impact dissolution rates through time (Eq. 2). Secondary mineral rates at the start of simulations denote net dissolution, though at rates orders of magnitude slower than plagioclase dissolution, for the first few days of simulation time as dilute solutes are undersaturated with respect to halloysite. As Al^{3+} and $SiO_2(aq)$ activities increase due to plagioclase dissolution, halloysite transitions to net precipitation; however, due to the low intrinsic rate constant, net precipitation rates are initially subdued. Precipitation rates increase to a maximum value roughly 2.5 months into the simulation as solutes become orders of magnitude oversaturated with respect to halloysite and then subsequently decrease over the rest of the simulation.

Instantaneous weathering incongruence is shown as the ratio of rates of halloysite precipitation to plagioclase dissolution in figure 2b. At the start of the simulation, weathering is fully congruent (ratio of zero) until the initiation of halloysite precipitation. Increasing halloysite precipitation results in an overshoot in weathering incongruence, whereby more halloysite precipitates than predicted based on equilibrium reaction stoichiometry to compensate for initial congruent weathering. Following this overshoot, the ratio of halloysite precipitation to plagioclase dissolution approaches the stoichiometric balance of ~0.6 from the equilibrium reaction,

$$1.66Plag(An20) + 2CO_2(g) + 3H_2O \leftrightarrow Halloysite + 0.33Ca^{2+} + 1.33Na^{+} + 2.66SiO_2(aq) + 2HCO_3^{-} \quad (8).$$

We note that even as dissolution/precipitation rates decrease through time as the system approaches thermodynamic equilibrium, this stoichiometric ratio is maintained.

Simulated Ca^{2+} concentrations (fig. 2c) are influenced only by plagioclase dissolution, as Ca^{2+} is not incorporated into halloysite. Concentrations rise rapidly over the first ~6 months of simulation, after which increases attenuate as dissolution rates decrease. Maximum concentrations of ~45 μM are reached at roughly 500 years of simulation as the system approaches equilibrium, and this final concentration is dependent on the specified open-system pCO_2 through its control on initial and equilibrium pH (5.0 and 8.9, respectively) (Winnick and Maher, 2018). The evolution of Li^+ differs from Ca^{2+} due to the incorporation of Li^+ into precipitating halloysite. Concentrations are therefore strongly dependent on the partition coefficient (P_{Li}) as shown in fig. 2d. In the initial stages of weathering, Li^+ increases similarly across the range of partition coefficients, and after halloysite precipitation initiates, partition coefficient simulations diverge. Simulations with low partition coefficients in which relatively little of the Li^+ released during plagioclase dissolution is incorporated into halloysite result in rapidly increasing concentrations, similar to Ca^{2+}. In contrast, simulations with high partition coefficients result in a transient decrease in Li^+ reflecting the overshoot in weathering incongruence, followed by slowly increasing values as the system approaches equilibrium.

Partition coefficients also control the evolution of δ^7Li (fig. 3). When the partition coefficient is low and little Li^+ is incorporated into clays, the extent of fractionation is reduced, and δ^7Li_{diss} is similar to δ^7Li_{plag}. When the partition coefficient is large, δ^7Li_{diss} reflects the full 18‰ fractionation factor. Additionally, the transient weathering incongruence overshoot results in transiently elevated δ^7Li_{diss} values, which subsequently approach steady-state values. We note that, similar to instantaneous weathering incongruence, δ^7Li_{diss} reach steady-state values at roughly 6 months, which is long before the system as a whole approaches equilibrium. Rather than overall reaction progress, δ^7Li_{diss} reflects the approach to stoichiometric balance between plagioclase dissolution and halloysite precipitation.

In figure 3b, we show the relationship between δ^7Li_{diss} and f_{Li}, which in this case reflects the weathering congruence of Li^+ (combining both congruence changes in the approach to stoichiometric balance and P_{Li}). Steady-state δ^7Li_{diss} values (colored circles reflecting plateau values in fig. 3a) are linearly related to f_{Li}, similar to the 'batch-reactor' relationship described by

Bouchez and others (2013) and Dellinger and others (2015). The approach to steady-state δ^7Li_{diss} values within each P_{Li} simulation (colored lines) involves a stronger dependence on f_{Li} than steady-state values, which is due to the previously described overshoot in halloysite precipitation rates and weathering incongruence. Global riverine δ^7Li_{diss} observations from Dellinger and others (2015) are also shown and fall roughly in line with CrunchFlow simulations, with the exception of flood-plain dominated environments as described above, which require sustained open-system clay uptake as in Maffre and others (2020).

Weathering Profiles – Chronosequence (Scenario 2)

Reactive transport simulations of weathering profiles have been presented in a number of previous studies (Maher et al., 2009; Maher, 2010, 2011; Moore et al., 2012; Lebedeva and Brantley, 2013; Lawrence et al., 2014; Pandey and Rajaram, 2016; Heidari and others, 2017; Winnick and Maher, 2018; Jung and Navarre-Sitchler, 2018; Perez-Fodich and Derry, 2019; Golla et al. 2021). We limit this discussion to a brief overview of general weathering characteristics and refer readers to these references for further details. Results from our simulations are shown in figure 4 with a P_{Li} value of 0.9, where colored lines are used to represent the evolution of solid and aqueous profiles through time.

At the beginning of the simulation, the solid profile represents fresh, unweathered bedrock. For this choice of initial conditions, the spatial evolution of aqueous solutes and mineral reaction rates generally resemble the temporal evolution of the batch reactor experiments presented above. Plagioclase weathering begins immediately at the surface as dilute, weakly acidic (pH = 5.0) waters infiltrate, releasing Ca^{2+} and Li^{+} (along with other reaction products not shown) into solution. Halloysite precipitation begins at ~20 cm depth, reflecting the water travel times necessary to significantly oversaturate solutes with respect to halloysite, as in figure 2a. This balance of dissolution/precipitation is reflected in weathering incongruence (fig. 4c), where incongruence increases at the depth where halloysite precipitation becomes significant, reaches a maximum at ~0.75 m, and approaches the stoichiometric balance of plagioclase dissolution to halloysite precipitation (0.6) at roughly 2 m. As with the batch reactor experiments (fig. 3a), δ^7Li_{diss} tracks weathering incongruence, approaching enriched steady-state values at ~1 m (fig. 4f).

As the simulation moves through time, plagioclase is progressively depleted from the shallow depths, with this pattern propagating downward through the profile. Plagioclase is largely depleted from the 10 m weathering profile by the end of the simulation at 10^6 yrs; however, small amounts remain as the surface area term in equation (2) limits kinetic rates of dissolution. Halloysite builds up in the profile from top to bottom due to progressive precipitation, though, precipitation is limited in the top 20 cm due to slow kinetics. Additionally, halloysite transitions to dissolution when plagioclase is sufficiently depleted at the top of the profile. Solute profiles of $[Ca^{2+}]$ and $[Li^{+}]$ generally track the evolution of mineral profiles on these long timescales. Specifically, decreases in $[Ca^{2+}]$ and $[Li^{+}]$ at a given depth through time match plagioclase depletion and are related to reduced mineral surface area and subsequent decreasing dissolution rates.

Weathering incongruence and subsequent δ^7Li_{diss} approach steady-state values at increasing depths through time. This is tied to reduced plagioclase dissolution rates in the upper profile as primary mineral is depleted, resulting in greater travel times needed to initiate halloysite precipitation and approach δ^7Li_{diss} steady-state values. Despite these longer δ^7Li_{diss} length scales, steady-state values are approached by the bottom of the 10 m profile until plagioclase is depleted throughout the profile at 10^6 yrs. When plagioclase has been depleted, the weathering regime transitions to net clay dissolution throughout the profile, and δ^7Li_{diss} values become more negative, resembling the clay values that were precipitated earlier in the simulation. However, through time, very small rates of plagioclase dissolution cause δ^7Li_{diss} to evolve during transport and fall between bedrock and clay values by the bottom of the profile. This last timestep also coincides with low $[Li^{+}]$ due to slow dissolution kinetics of halloysite. These results are consistent with some behavior shown in tropical weathering environments (Lara and others, 2022) in which δ^7Li_{diss} are extremely low in weathered soils (though absolute values of measured pore waters and clay δ^7Li would require extremely low P_{Li} values and large clay fractionation) and are disconnected from stream environments as deeper weathering and higher $[Li^{+}]$ from primary mineral dissolution seemingly overwhelm clay dissolution.

Uplift/Erosion (Scenario 3)

As described previously, we simulate a range of both uplift/erosion and flow rates to capture a broad range of weathering intensity regimes. Across this suite, 30 unique WI regimes were tested, varying from 2.7×10^{-5} to 0.93. Illustrative examples of low weathering intensity (high uplift/erosion, low flow), moderate weathering intensity (comparable uplift/erosion and flow), and high weathering intensity (low uplift/erosion, high flow) environments are compared in figure 5. We note that in figure 5, only the low weathering intensity simulation reaches steady-state with respect to the mineral abundances and fluid compositions, as discussed below.

Under low weathering intensity, the supply of fresh bedrock overwhelms chemical denudation, and weathering profile solid compositions reflect bedrock values throughout the simulation (fig. 5a-c). In the illustrative example, plagioclase is very slightly depleted within the top <1 m. Based on our definition of the regolith weathering zone (porosity >101% bedrock porosity), this profile corresponds to a regolith depth of 5 cm, and solute concentrations are taken from this depth when comparing between weathering intensity simulations. Similar to solid composition, weathering incongruence and δ^7Li_{diss} profiles do not vary significantly with depth or through the course of the simulation. As water infiltrates through the 1D un-weathered bedrock profile, the behavior is largely comparable to the batch reactors; however, the approach to stoichiometric weathering incongruence and steady-state δ^7Li_{diss} values occur at depths below the defined regolith weathering zone. As a result, δ^7Li_{diss} values from this simulation are ~0‰ at the weathering zone depth of 5 cm.

When erosion rates and chemical denudation are comparable under moderate weathering intensity, weathering profiles evolve with depth throughout the duration of the simulation. Through time, plagioclase is depleted and halloysite is precipitated in the upper portion of the profile. In contrast to the no-erosion simulation in figure 4, plagioclase reaction fronts are condensed, reflecting the additional uplift flux of bedrock. Similarly, the erosion of material from the surface eliminates the diminished accumulation of halloysite in the top few cm's of the profile as compared to figure 4. In figure 5e-h, regolith depth reaches a maximum of ~8 m in 10^6 yrs. As with the no-erosion case, weathering incongruence and δ^7Li_{diss} track the evolution of the solid profile, with an increasing length needed to approach stoichiometric incongruence and steady-state δ^7Li_{diss} values. Throughout the simulation, both incongruence and δ^7Li_{diss} approach steady-state maximum values at the base of the weathered regolith profile. At 10^6 years when plagioclase is completely depleted from the top of the profile, clay dissolution occurs over the

top ~1 m during infiltration; however, the associated low δ^7Li_{diss} values are quickly overwhelmed by the influx of lithium when waters reach the plagioclase dissolution front.

Under high weathering intensity, the lack of uplift/erosional forcing results in the depletion of primary minerals and accumulation of secondary minerals as shown in figure 5i-l. We note that while patterns resemble those presented in figure 4, a few differences exist largely related to differences in infiltration rate (5 m/yr in fig. 5 v. 0.5 m/yr in fig. 4). As a result of these high infiltration rates, overall weathering intensity increases, causing plagioclase depletion almost uniformly throughout the profile rather than in a discrete reaction front. Another important difference is the approach to bedrock conditions at 10 m depth, which reflects the imposed uplift/erosion boundary condition. Similar to figure 4, weathering incongruence profiles track the solid profile composition. At early time, weathering incongruence remains low over the first ~1 m of infiltration before approaching stoichiometric incongruence coincident with the approach to steady-state δ^7Li_{diss} values; this is due to fast infiltration rates which result in reduced water travel times in comparison to figure 4. At simulation time 10^5 yrs, very little plagioclase remains throughout the profile. As a result, while weathering incongruence reaches stoichiometric balance by the bottom of the profile, overall plagioclase dissolution rates and subsequent Li release from primary minerals are so low that δ^7Li_{diss} reflects a mixture of halloysite dissolution at the top of the profile (negative incongruence) and plagioclase dissolution/halloysite precipitation at the bottom. Following the complete denudation of plagioclase from the upper profile by $2.5x10^5$ yrs, weathering incongruence and δ^7Li_{diss} remain low throughout the profile.

Erosion/Uplift with Chlorite (Scenario 4)

The introduction of soluble chlorite minerals changes lithium weathering dynamics within our simulations. In these simulations, the rapid vermiculitization of chlorite releases Li congruently. As a result, dissolved Li concentrations are high (~1 μM), and δ^7Li_{diss} values are close to bedrock values when chlorite is present. Plagioclase dissolution and subsequent halloysite precipitation continue to a reduced degree in the presence of chlorite but have little effect on Li concentrations and isotopes due to the relatively small amount of Li released and removed in comparison to vermiculitization.

649 The temporal evolution of 1-D weathering profiles with chlorite can be seen in the high
650 weathering intensity panels in figure 6. Due to its high solubility, chlorite is rapidly weathered to
651 vermiculite, involving the leaching of Mg^{2+} and Li^{+} throughout the weathering profile over
652 <1000 years of simulation. When chlorite is present in the profile, Li concentrations are high and
653 δ^7Li_{diss} resemble bedrock values. However, after the rapid depletion of chlorite, the high
654 weathering intensity simulations behave similar to those in figure 5i-l. Plagioclase is depleted
655 from the profile over timescales of 10^5 yrs, after which clay dissolution is the primary contributor
656 to Li concentrations and δ^7Li_{diss}.
657 Similar dynamics are observed under moderate weathering intensity (fig. 6 e-h). Despite
658 elevated uplift/erosion rates relative to the high weathering intensity simulation, protolith chlorite
659 is still depleted from the profile in $<10^5$ years. As before, once chlorite is depleted, the temporal
660 evolution of the profile behaves as in figure 5 e-h, in which incongruent plagioclase weathering
661 leads to high δ^7Li_{diss} values and Li concentrations on the order of 10^2 nM, both of which are
662 dependent on P_{Li}.
663 In the low weathering intensity scenario, uplift/erosion rates are sufficiently high that
664 significant chlorite mineral concentrations remain within the weathering zone throughout the
665 simulation (fig. 6 a-d). In other words, under high enough uplift/erosion and low enough water
666 infiltration rates, chlorite becomes kinetic- rather than supply limited. As a result, Li
667 concentrations remain high ($\sim10^3$ nM) and δ^7Li_{diss} reflect bedrock values throughout 1 Myr of
668 simulation within the shallow weathering zone.
669 These results are broadly consistent with field studies demonstrating deep chlorite
670 'vermiculitazation' or the leaching and oxidative weathering of octahedral cations (Mg^{2+}, Fe^{2+})
671 relative to plagioclase depletion depths under low to moderate erosion rates, along with the
672 presence of fresh chlorite in shallow soils under high erosion rates (Sullivan and others, 2016;
673 Gu and others, 2020). Mineralogic profiles in tropical weathering environments have also
674 demonstrated the complete depletion of chlorite in weathered saprolite and soil (Murphy and
675 others, 1998).
676
677 *Weathering Intensity, δ^7Li, and $[Li^+]$*
678

679 In figure 7, we compare the relationships among δ^7Li_{diss} and both weathering intensity
680 and $[Li^+]$ from Scenarios 3 and 4 and global observations from Dellinger and others (2015) and
681 references therein. Figure 7 shows model output at the 500,000-year timestep for simulations
682 with a P_{Li} value of 0.9 (maximum isotopic offset of ~17‰). We also discuss the sensitivity of
683 model results to variable P_{Li} values in Appendix A. This timestep choice allows for the
684 development of deeply weathered profiles under low erosion conditions, characteristic of tropical
685 craton environments; at earlier timesteps, many high WI simulations have not fully transitioned
686 to clay dissolution. In both our simulations without and with the inclusion of chlorite, δ^7Li_{diss}
687 follows a parabolic pattern with low (bedrock-like) values at both high and low weathering
688 intensity. In agreement with observations and as previously theorized, low δ^7Li_{diss} at high
689 weathering intensity is due to long mineral residence times that result in the depletion of primary
690 minerals and the dominance of secondary mineral dissolution across both classes of simulation.
691 However, despite similar δ^7Li_{diss} values at low weathering intensity, the mechanisms underlying
692 this behavior vary between simulations. When chlorite is not included in our mineral
693 assemblage, low weathering intensity δ^7Li_{diss} values are due to rapid fluid travel times through
694 the shallow weathering zone that limit secondary mineral precipitation. In contrast, low
695 weathering intensity δ^7Li_{diss} values with the inclusion of chlorite are caused by the active
696 weathering of soluble, Li-rich minerals which overcome clay precipitation uptake and are
697 sustained only through the rapid uplift supply of fresh bedrock.
698 As a result of these differing mechanisms, the relationships between δ^7Li_{diss} and $[Li^+]$
699 differ between the two classes of simulation. When chlorite is not included, δ^7Li_{diss} is low at low
700 $[Li^+]$ and high at high $[Li^+]$. Under high weathering intensities when clay dissolution dominates
701 Li release, low clay solubilities and lack of a precipitating phase result in low $[Li^+]$ and δ^7Li_{diss}.
702 Under low weathering intensities, fluid travel time limitations on secondary mineral precipitation
703 also limit primary mineral dissolution, and $[Li^+]$ is unable to accumulate. Only under moderate
704 weathering intensities when incongruent weathering (eq. 8) can occur within the weathering zone
705 does $[Li^+]$ approach equilibrium concentrations; however, we note that even these $[Li^+]$ values
706 are roughly an order of magnitude less than maximum riverine $[Li^+]$ observations. When chlorite
707 is included, simulations produce the observed parabolic relationship between δ^7Li_{diss} and $[Li^+]$, as
708 the dissolution of chlorite at low weathering intensities allows for $[Li^+]$ to accumulate in solution
709 and approach the range of maximum observed $[Li^+]$ values (10^3 nM).

Lastly, figure 8 shows simulated δ^7Li_{sus}, taken as the isotopic composition of lithium in plagioclase and halloysite (and chlorite when included) in the eroding uppermost model domain cell (0.025 m) at the 250 ka time-step, in comparison to values from Dellinger and others (2017). We exclude low-Li quartz eroded from the surface in our calculation, as Dellinger and others (2017) report values from the fine fraction of sediment. Figure 8 shows results from both classes of simulation (with and without chlorite), between which the overall pattern does not vary. At low weathering intensity, the erosion of minimally-weathered bedrock from the profile surface results in bedrock-like δ^7Li_{sus} values that vary across our simulations based on initialized δ^7Li values of halloysite in bedrock. Above weathering intensities of ~0.01, plagioclase (and chlorite) is increasingly depleted from eroding surfaces in our simulations. As a result, δ^7Li_{sus} values decrease, approaching δ^7Li values of precipitating clay, which are dependent on P_{Li}. Observational data follow this general trend as well, with low δ^7Li_{sus} values at high weathering intensity falling roughly in the center of our simulation ranges.

DISCUSSION

The results from our series of CrunchFlow weathering simulations suggest a number of important controls on Li systematics and their relationship to weathering regimes. We first compare model output to global river observations and review the primary drivers of Li isotope and concentration signals including weathering congruence, mineral composition, mineral residence times in regolith, and fluid travel times. Next, we discuss the inability of fluid travel time controls to capture observed relationships between weathering regime, δ^7Li_{diss}, and $[Li^+]$. Instead, we show that the incorporation of soluble, Li-rich chlorite phases in our weathering experiments produces signals consistent with global observations. Additionally, we describe an alternative hypothesis outside the scope of CrunchFlow simulations that geothermal water contributions may also link weathering regimes and Li isotopes and concentrations in river systems. Lastly, we discuss model limitations along with need for future studies to evaluate these hypotheses in the field.

Insights from Reactive Transport Simulations

With a relatively simple representation of kinetic lithium isotopic fractionation during clay precipitation, we are able to capture a number of key features of global riverine Li data. First, as shown in figure 3, the simulated offset between δ^7Li_{diss} and $\delta^7Li_{bedrock}$ is a function of the fraction of Li dissolved that remains in solution, f_{Li}. This relationship is linear, matching general 'batch reactor'-style behavior observed across the Amazon basin (Dellinger and others, 2015). As our analysis is focused on hillslope processes, we do not simulate the scavenging of dissolved Li by extant secondary phases as is theorized to occur in floodplains. The result is that we do not capture significantly elevated δ^7Li_{diss} values (20-35‰), attributed to 'Rayleigh-style' floodplain processes (fig. 3b), though transient overshoots in weathering incongruence during initial clay precipitation capture similar style behavior.

Our relatively simple weathering mineralogy is also able to capture global ranges of riverine $[Li^+]$ from ~10^0-10^3 nM, though we note that simulated concentrations above 200 nM require the inclusion of a soluble, Li-rich mineral such as chlorite or lithium-bearing alkali amphibole. In particular, across simulations both with and without chlorite, the transition from clay dissolution to primary mineral dissolution between high and medium weathering intensity environments captures the observed increase in $[Li^+]$ from ~10^0 to ~10^2 nM along with decreases in δ^7Li_{diss} values. Simulations with high chlorite-derived $[Li^+]$ are discussed in more detail in the following section.

Our simulations also clarify the distinct controls of fluid travel time and mineral residence time on Li systematics. Similar to previous reactive transport studies, δ^7Li_{diss} during incongruent weathering increases with increasing fluid travel time (Wanner and others, 2014; Bohlin and Bickle, 2019; Golla et al. 2021). We note, however, that our simulations reach maximum δ^7Li_{diss} as incongruent weathering approaches a stoichiometric steady-state, while solute concentrations continue to increase. This is occurs on much shorter timescales than those required for the system to approach a meta-stable equilibrium between dissolving and precipitating phases when net reaction rates approach zero and solute concentrations remain constant. This travel time dependence broadly matches concentration-discharge behavior observed in streams, in which high seasonal discharge periods associated with faster fluid travel times exhibit lower $[Li^+]$ and δ^7Li_{diss} as compared to low discharge periods (Lemarchand and others, 2010; Manaka and others, 2017). We demonstrate qualitative concentration-discharge

771 dynamics associated with our model output assuming a gamma-function travel time distribution
772 in Appendix B.

773 In contrast, mineral residence times control the dominant weathering reactions, as
774 primary minerals are sequentially depleted from regolith with increasing mineral residence time.
775 This has previously been suggested to control the transition from primary mineral dissolution to
776 secondary mineral dissolution at high weathering intensities (Bouchez and others, 2013), and we
777 extend this framework to demonstrate potential transitions in dominant primary mineral reactions
778 and associated Li sources at low weathering intensities. We also note that mineral residence
779 times do not directly impact weathering congruence in our simulations except through these
780 distinct transitions in weathering mineralogy. This is in contrast to previous studies in which
781 relative rates of primary mineral dissolution and secondary mineral precipitation are directly
782 dependent on mineral residence times (Chamberlain and others, 2005; Ferrier and Kirchner,
783 2008; Bouchez and others, 2013). While halloysite does not significantly accumulate under short
784 mineral residence times within our low WI simulations (fig. 5b), relative rates of halloysite
785 precipitation are still proportional to plagioclase dissolution integrated across the modeling
786 domain as enforced through the affinity-dependence terms in mineral precipitation/dissolution
787 rates (eq. 2). We offer a linkage between mineral residence time controls, fluid travel times and
788 associated weathering congruence by evaluating solute exports from the defined regolith zone
789 (gray shading in fig.'s 5 and 6), representing preferential flow through more porous regolith and
790 soil media relative to unweathered bedrock. This connection is implicit in previous studies, and
791 we discuss its incompatibility with observations of high $[Li^+]$ under low WI in the following
792 section.

793 CrunchFlow simulations also support the hypothesis that mineral residence times are
794 responsible for the broad trends between observed δ^7Li_{sus} and weathering intensity (Dellinger
795 and others, 2017; fig. 8). Specifically, at low weathering intensities when mineral residence
796 times are short, δ^7Li_{sus} largely represents contributions from primary minerals as interpreted by
797 Dellinger and others (2017). With increasing weathering intensity and the depletion of primary
798 minerals from the shallow, actively-eroding zone of regolith, δ^7Li_{sus} transitions to values
799 reflecting secondary minerals. We note that our simulations predict a much wider spread in
800 δ^7Li_{sus} at high weathering intensities than observed. This primarily reflects the fact that low

801 $(Li/Al)_{sec}/(Li/Al)_{prim}$ (i.e. P_{Li}) are not observed at low weathering intensities (Dellinger and
802 others, 2017).
803
804 *Weathering Intensity Controls on* δ^7Li_{diss}
805
806 As described by both observations and theoretical considerations, δ^7Li_{diss} is related to WI
807 through a parabolic relationship (fig. 1, fig. 7e). Previous studies hypothesize that low δ^7Li_{diss}
808 values observed in low WI environments are caused by short fluid and mineral residence times
809 that inhibit secondary mineral precipitation relative to primary mineral dissolution, thereby
810 limiting the extent of Li fractionation (Bouchez and others, 2013; Dellinger and others, 2015).
811 Our CrunchFlow simulations demonstrate two potential issues with this hypothesis. First, the
812 treatment of weathering profiles within a multi-component RTM framework in which reaction
813 rates are based on solution chemistry suggests that there is no intrinsic connection between
814 mineral residence time and weathering congruence. Models that include this connection
815 implicitly assume that all weathering occurs within regolith, or mineral-depleted weathering
816 profiles, such that travel times are dependent on regolith thickness. However, this does not
817 account for infiltration of waters into relatively un-weathered bedrock, for example via fracture
818 flow. As shown in Appendix B, riverine δ^7Li_{diss} may reflect a lack of secondary mineral
819 precipitation depending on the travel time distributions and mean travel times that dictate the
820 proportional contribution of these 'young', non-evolved waters (Kirchner, 2016; Jasechko and
821 others, 2016). However, for travel times to result in the observed δ^7Li_{diss}-WI relationships, young
822 water fractions would need to be highest in low WI environments. This connection between
823 travel times and erosional environments is an open question; however, we note that this is in
824 direct contrast to Jasechko and others (2016), who suggest relatively low proportions of 'young'
825 waters in high slope environments associated with low WI.
826 Second, short fluid travel times that limit secondary mineral precipitation also limit
827 primary mineral dissolution and overall reaction progress. The result is that under short fluid
828 travel times, simulated $[Li^+]$ is extremely low, on the order of <10 nM. This is in direct conflict
829 with observations that show the highest $[Li^+]$ in low WI and rapidly eroding environments, on
830 the order of 10^3 nM (Dellinger and others, 2015; Pogge von Strandmann and Henderson, 2015).
831 Fluid travel times, are therefore unable to capture observed parabolic relationships between

832 δ^7Li_{diss} and [Li^+] as shown in figure 7. Given that observed low WI [Li^+] on the order of 10^3 is
833 difficult to account for with typical granitic Li concentrations and plagioclase mineral solubility,
834 we suggest that low WI observations instead represent Li release from soluble, Li-rich minerals
835 such as chlorite.

836 Under this hypothesis, only low WI and short mineral residence times within the
837 weathering zone are able to maintain chlorite in significant concentrations. Our simulated
838 chlorite weathering profiles broadly match a recent comparison of 'vermiculitization' profiles
839 under high, medium, and low erosion rates in which protolith chlorite concentrations are
840 maintained in shallow soils only under high erosion rates (1-3 mm/yr; Gu and others, 2020). Due
841 to the high solubility and relatively high Li concentrations of chlorite, low δ^7Li_{diss} results from
842 high dissolved Li concentrations that overwhelm uptake by secondary mineral precipitation. In
843 our simulations, the transition from low to moderate weathering intensity then results in a change
844 in the dominant Li weathering reaction from chlorite dissolution to plagioclase dissolution,
845 which is an inherently more incongruent weathering reaction for Li. This mechanism, in contrast
846 to fluid travel times, predicts parabolic relationships between δ^7Li_{diss} and both WI and [Li^+]
847 consistent with observations, as shown in figure 7. We note that while our simulations are
848 limited to idealized representations of chlorite leaching, this overall pattern is characteristic of a
849 general situation in which Li exists at relatively higher concentrations in a more soluble mineral
850 within the bedrock assemblage such as lithium-bearing alkali amphiboles.

851 We also suggest that while our simulations only involve steady surface erosion rates,
852 these dynamics should theoretically apply to environments in which transient mass wasting
853 events occur as well. Periodic mass wasting events would expose fresh bedrock and allow for
854 highly weatherable minerals to be maintained close to the surface.

855 With respect to riverine observations, low WI primarily represents the weathering of
856 shale (Dellinger and others, 2015; Beni River) and metamorphically-altered (Pogge von
857 Strandmann and Henderson, 2015; New Zealand) bedrock, which typically contain Li-rich, ferro-
858 magnesian minerals such as chlorite. As mentioned above, the inclusion of chlorite brings our
859 bedrock Li concentrations in line with typical shale values (Holland, 1984) and bedrock values
860 observed in the Beni River watershed (Dellinger and others, 2015). Further, a study of Amazon
861 tributary sediments found high stream chlorite and illite contents (~30%) in the Andean Madeira
862 River (of which the Beni is a tributary) suggesting rapid erosion of soluble minerals (Gibbs,

1967). Additionally, chlorite presence decreases significantly along the Andean Ucayali river and is significantly lower in Amazon shield rivers (Irion, 1983; Gibbs, 1967), also in line with our hypothesized mineralogic controls. While we demonstrate the potential for chlorite weathering to explain observed relationships between weathering intensity, δ^7Li_{diss}, and $[Li^+]$, only very limited inferences have been drawn regarding chlorite contributions to Li weathering in actively eroding field environments (Golla et al. 2021). Thus, targeted studies are needed to evaluate whether or not chlorite or other highly soluble, Li-bearing minerals are responsible for high $[Li^+]$ and low δ^7Li_{diss} in low WI environments. Other mechanisms such as geothermal water contributions may also be consistent with the parabolic relationships in figure 7 e-f, as we describe in the following section.

Alternative Hypothesis: Geothermal Waters

Our analysis confirms that changes in weathering zone mineralogy as modulated by weathering intensity are consistent with global patterns of riverine lithium concentrations and isotopes; however, other mechanisms may also contribute to observed patterns. One possibility is that geothermal waters play an increasingly important role in Li fluxes under low weathering intensity conditions. A number of studies have observed high $[Li^+]$ (10^{-1}-10^4 μM) often coincident with bedrock-like δ^7Li_{diss} values in geothermal springs (Millot and Negrel, 2007; Millot and others, 2007, 2010b, 2012; Bernal and others, 2014; Godfrey and Álvarez-Amado, 2020). This has been attributed to high reaction temperatures that alter dominant clay stability to phases that incorporate less Li and reduce fractionation factors (Verney-Carron and others, 2015; Pogge von Strandmann and others, 2016). If relative contributions of geothermal waters are highest in low weathering intensity regimes, for example due to active tectonic uplift (Chamberlain and others, 2002), this could result in the parabolic δ^7Li_{diss} patterns of figure 7e-f: *(1)* At high weathering intensity, clay dissolution results in low $[Li^+]$ and low δ^7Li_{diss}; *(2)* at moderate weathering intensity, where geothermal waters do not contribute significantly to solute fluxes, primary mineral dissolution coupled with secondary mineral precipitation results in moderate $[Li^+]$ and high δ^7Li_{diss}; and *(3)* at low weathering intensity, where geothermal waters contribute significantly to solute fluxes, the inhibition of secondary mineral precipitation during high temperature weathering results in high $[Li^+]$ and low δ^7Li_{diss}. Geothermal water

894 contributions in rapidly uplifting collisional orogens have been shown, for example, to control
895 radiogenic Sr budgets and overall solute fluxes in Himalayan rivers (Evans and others, 2001). As
896 with our chlorite hypothesis, this mechanism is consistent with riverine observations, and it is
897 supported by observations of geothermal waters; however, this has not been systematically
898 evaluated across WI gradients. Future studies targeting the potential role of geothermal waters
899 and evaluating these competing hypotheses may shed important light on the mechanistic
900 relationships between weathering environments and Li systematics. In particular, future studies
901 are needed that target low WI environments including the detailed characterization of weathering
902 zone mineralogy (e.g. the presence of soluble Li-rich minerals, mineralogical P_{Li} values for
903 secondary phases, and fluid travel times).
904
905 *Limitations of Approach*
906
907 One primary limitation of our methodology is that the partition coefficient P_{Li} is set via
908 mineral stoichiometries rather than evolving as a function of fluid chemistry. Mechanisms for the
909 latter may include: competing clay phases, recrystallization/Ostwald ripening, sorption-
910 desorption, and concentration-dependent trace element incorporation. In modeling Li uptake
911 during clay formation, we chose a simplistic representation of halloysite Li-uptake such that
912 mineral solubility was only dependent on Si and Al concentrations rather than base cation
913 concentrations. This allows us to systematically vary P_{Li} across the full 0-1 range through
914 specific trace Li concentration without inducing time- or depth-dependent changes in P_{Li} within
915 individual simulations. However, it also limits the ability to forward-model or predict δ^7Li
916 behavior at a specific site without local constraints on bedrock and secondary phase lithium
917 concentrations. In particular, it will require extensive field characterization in order to accurately
918 simulate the effects of evolving clay stability on Li isotope dynamics. Similarly, we do not
919 include any dependence of instantaneous P_{Li} on [Li^+], as has been noted experimentally
920 (Decarreau and others, 2012) and included in other reactive transport frameworks (Wanner and
921 others, 2014; Bohlin and Bickle, 2019). The incorporation of these dynamics would not change
922 the relationship between f_{Li} and δ^7Li_{diss} at steady-state (fig. 3b, filled circles) but would change
923 the approach to steady state (fig. 3b, colored lines). Additionally, P_{Li} dependence on [Li^+] may
924 extend the reaction timescales over which δ^7Li_{diss} increases. While this may allow for more

realistic fluid travel times to support δ^7Li_{diss} observations in low WI environments, it would still result in low [Li^+], in conflict with observations.

Catchments are also complex 3-dimensional systems with variable distributions of fluid travel times. As such, rivers may integrate a wide range of flow paths with different f_{Li} and resulting δ^7Li_{diss}, even in the absence of appreciable floodplain exchange. In addition, local heterogeneity may impact the efficiency of reactions relative to that shown here for initially homogeneous domains (Pandey and others, Jung and Navarre-Sitchler, 2018). In spite of the large- and small-scale heterogeneities that exist in catchment and regolith profiles, respectively, the general trends presented in the 1-D simulations here are still applicable (Maher, 2011; Pandey and others, Jung and Navarre-Sitchler, 2018). Thus, although the simulations do not capture full complexity of catchments and initial conditions, they do represent a broad spectrum of flow rates, erosion rates and weathering rates and thus provide general insights into potential behavior of Li isotopes.

CONCLUSIONS

In order to probe the relationships between weathering intensity and Li isotope systematics, we incorporate Li isotope fractionation processes into CrunchFlow reactive transport simulations of weathering granite. Using a parsimonious effective kinetic fractionation parameterization, our simulations capture broad patterns in observed relationships between δ^7Li_{diss} and the fraction of dissolved Li remaining in solution following secondary mineral precipitation. Upland weathering profiles are simulated across a range of weathering intensities by varying water infiltration and bedrock uplift/erosion rates. Simulations produce a parabolic relationship between δ^7Li_{diss} and weathering intensity similar to global observations, controlled by a combination of fluid travel times and mineral residence times in the weathering zone. However, fluid travel and mineral residence time controls alone are unable to capture high observed Li concentrations under low weathering intensity conditions: short fluid travel times that limit clay precipitation also limit primary mineral dissolution and solute accumulation. Instead, we demonstrate how mineral residence times may regulate the dominant Li weathering reactions, where the weathering of soluble, Li-rich minerals may only be sustained with the rapid supply of fresh bedrock. This mineralogic control on Li isotope systematics is able to capture

parabolic relationships between δ^7Li_{diss} and both weathering intensity and Li concentrations. We suggest that as a viable hypothesis, this mineralogic control may be tested against other possible mechanistic ties between weathering regimes and Li systematics such as varying contributions from geothermal waters.

The refinement of a theoretical framework for Li isotope systematics may provide for more accurate reconstructions of weathering dynamics in the past. In particular, direct links between Li-specific congruence (P_{Li}) and overall weathering congruence need to be established in order for Li isotopes to serve as a direct proxy of weathering intensity. Additionally, based on the parabolic relationships described above, tectonic uplift and attendant shifts in weathering may be result in either increasing or decreasing δ^7Li_{diss} values depending on the background weathering intensity. Thus, understanding the mechanistic connections between uplift and δ^7Li_{diss} may allow for more direct hypothesis evaluation, for example, through comparisons of proxy δ^7Li with coeval records of hydrologic shifts or changes in depositional environment mineralogy along active orogens that may indicate changes in fluid and mineral residence times.

ACKNOWLEDGEMENTS

We thank Daniel Ibarra, Jeremy Caves, and Friedhelm von Blanckenburg for useful comments and conversations, along with the Associate Editor and two anonymous reviewers whose comments and suggestions improved an earlier version of this manuscript. This work was supported by the National Science Foundation (EAR-1254156) to K.M. The authors will make updated CrunchFlow software source code and all input files used in this analysis available on request.

Appendix A: Weathering Reaction Sensitivity Analysis.

To demonstrate the sensitivity of the presented simulations to assumptions of prescribed P_{Li} values in Figure 8 and to our idealized reaction network, we present analyses showing:

A1) How δ^7Li_{diss} varies as a function of weathering intensity and [Li] for a range of P_{Li} values, and
A2) How the use of a 2:1 clay rather than 1:1 halloysite does not impact apparent fractionations.

A.1 - To show the sensitivity of δ^7Li_{diss} to weathering intensity and [Li], we present an altered version of Figure 7e,f in which simulations are color-coded by prescribed P_{Li} (0.08, 0.53, and 0.99). As P_{Li} primarily impacts the maximum extent of δ^7Li_{diss} increase during incongruent plagioclase weathering, the effect of lowering P_{Li} is to flatten the parabolic curves of δ^7Li_{diss} v.

WI and δ^7Li_{diss} v. [Li]. In other words, smaller P_{Li} values result in lower ranges of δ^7Li_{diss} variability. Additionally, P_{Li} values impact the concentrations of Li during incongruent and clay weathering along with δ^7Li_{clay} values. This results in variable δ^7Li_{diss} at high weathering intensity when clay dissolution dominates and δ^7Li_{diss} matches δ^7Li_{clay} (figure A1a). It also results in $[Li^+]$ variability under both clay dissolution and incongruent weathering: as P_{Li} approaches 1, the difference in $[Li^+]$ under clay dissolution v. incongruent weathering decreases, causing a steeper left side of the parabolic curve in figure A1b.

A.2 - To demonstrate the insensitivity of our model simulations to alternative representations of clay mineralogy, we include batch reactor simulations similar to those presented in the main text where halloysite is replaced with a calcium beidellite (2:1 smectite group clay). Kinetic fractionation is implemented in the same manner, and we simulate a range of P_{Li} (0.08 – 0.93) values based on prescribed substitution of Li^+ for Ca^{2+} as shown in table A1. We chose to simulate a calcium rather than iron or magnesium 2:1 clay based on the lack of magnesium and iron in our primary mineral dissolution reaction (Plagioclase An20). Selected results corresponding to main text figures 2a,b,d and 3a are shown in figure A2. In comparison to our halloysite reaction, the simulation of beidellite alters the patterns of primary mineral dissolution and secondary mineral precipitation rates along with the steady-state weathering incongruence value representing stoichiometric balance of plagioclase dissolution and beidellite precipitation. Changes in the balance of rates are largely related to changes in reaction affinity as kinetic rate constants are unchanged from halloysite simulations. Weathering incongruence reflects represents the aluminum-normalized stoichiometry. As shown in figure A2, the evolution of δ^7Li_{diss} is identical to halloysite both as a function of time and of prescribed P_{Li}. Even though the model is simulating a different mechanisms of Li substitution (i.e. for substituted cations rather than structural aluminum), the P_{Li} value and kinetic fractionation factor together set δ^7Li_{diss} in the same manner as with structural substation for Al in halloysite.

Appendix B: Theoretical concentration-discharge dynamics.

In order to explore potential concentration-discharge dynamics encapsulated in our model simulations, we convolve idealized watershed travel time distributions with time-varying output from main text batch reactor simulations. Numerous studies have shown that times of high flow, either in response to transient infiltration events such as storms and snowmelt or sustained seasonal changes in precipitation, are associated with relatively lower mean travel times. To show how this may be manifested in stream solute data, we assume watershed travel time distributions may be represented by a gamma-type distribution as,

$$h(\tau) = \frac{\boldsymbol{\tau}^{\alpha-1}}{\left(\frac{\tau_m}{\alpha}\right)^{\alpha}\Gamma(\alpha)} e^{-\tau\alpha/\boldsymbol{\tau}_m},$$

where h is a weight for a given travel time $\boldsymbol{\tau}$, α represents a shape factor, and $\boldsymbol{\tau}_m$ is the mean travel time (e.g. Kirchner, 2016).

For the purposes of this exercise, we assume a shape factor of 1. We convolve travel time distributions with batch reactor experiment δ^7Li_{diss} for a range of mean travel time values by taking the weighted mean of Li concentration-weighted, time-dependent δ^7Li_{diss} values using

h(τ)*[Li](τ) as the weights. Figure B1 shows how the convolved δ^7Li_{diss} varies in response to mean travel times. As mean travel time decreases, the associated δ^7Li_{diss} decreases as well. This relationship is muted relative to the time v. δ^7Li_{diss} curves shown in Figure 3, due to the mixing across a wide range of travel times as discussed for solutes (e.g. Maher, 2011) and stable isotope ratios (Druhan & Maher, 2017) in previous papers. The largest changes are seen when mean travel times are in the vicinity of 1-3 months corresponding roughly to timescales of stoichiometric steady-state in the plagioclase dissolution – halloysite precipitation reaction series. Under these idealized scenarios, an increase in flow resulting in a reduction in mean travel time would cause a subsequent decrease in δ^7Li_{diss} values, consistent with field observations from a number of studies. Importantly, while the magnitude of δ^7Li_{diss} change is dependent on the shift and absolute value of mean travel time between low and high flow along with the shape factor, the direction of change is not. The precise relationship between mean travel time and discharge is not well characterized; however, interfacing this stable isotope reactive transport model with hillslope or watershed hydrologic models may facilitate concentration-discharge relationship predictions.

REFERENCES

Anghel, I., Turin, H. J., Reimus, P. W., 2002, Lithium sorption to Yucca Mountain tuffs: Applied Geochemistry, v. 17, p. 819-824.

Arnorsson, S., Stefansson, A., 1999, Assessment of feldspar solubility constants in water in the range 0 degrees to 350 degrees C at vapor saturation pressures: American Journal of Science v. 299, p. 173–209.

Bagard, M.-L., West, J. A., Newman, K., Basu, A. R., 2015, Lithium isotope fractionation in the Ganges-Brahmaputra floodplain and implications for groundwater impact on seawater isotopic composition: Earth and Planetary Science Letters, v. 432, p. 404-414.

Bernal, N. F., Gleeson, S. A., Dean, A. S., Liu, X. M., Hoskin, P., 2014, The source of halogens in geothermal fluids from the Taupo Volcanic Zone, North Island, New Zealand: Geochimica et Cosmochimica Acta, v. 126, p. 265-283.

von Blanckenburg, F., Hewawasam, T., Kubik, P. W., 2004, Cosmogenic nuclide evidence for low weathering and denudation in the wet, tropical highlands of Sri Lanka: Journal of Geophysical Research: Earth Surface, v. 109, F03008, 22 pp.

Bohlin, M. S. and Bickle, M. J., 2019, The reactive transport of Li as a monitor of weathering processes in kinetically limited weathering regimes: Earth and Planetary Science Letters, v. 511, p. 233-243.

Bouchez, J., von Blanckenburg, F., Schuessler, J. A., 2013, Modeling novel stable isotope ratios in the weathering zone: American Journal of Science, v. 313, p. 267-308.

Caves-Rugenstein, J. K., Ibarra, D. E., von Blanckenburg, F., 2019, Neogene cooling driven by land surface reactivity rather than increased weathering fluxes: Nature, v. 571, p. 99-102.

Chamberlain, C. P., Koons, P. O., Meltzer, A. S., Park, S. K., Craw, D., Zeitler, P., and Poage, M. A., 2002, Overview of hydrothermal activity associated with active orogenesis and metamorphism: Nanga Parbat, Pakistan Himalaya: American Journal of Science, v. 302(8), p. 726-748.

Chamberlain, C. P., Waldbauer, J. R., Jacobson, A. D., 2005, Strontium, hydrothermal systems and steady-state chemical weathering in active mountain belts: Earth and Planetary Science Letters, v. 238, p. 351-366.

Chan, L. H., Edmond, J. M., Thompson, G., Gillis, K., 1992, Lithium isotopic composition of submarine basalts: implications for the lithium cycle in the oceans: Earth and Planetary Science Letters, v. 108, p. 151-160.

Decarreau, A., Vigier, N., Pálková, H., Petit, S., Vieillard, P., Fontaine, C., 2012, Partitioning of lithium between smectite and solution: An experimental approach: Geochimica et Cosmochimica Acta, v. 85, p. 314-325.

Dellinger, M., Gaillardet, J., Bouchez, J., Calmels, D., Galy, V., Hilton, R. G., Louvat, P., France-Lanord, C., 2014, Lithium isotopes in large rivers reveal the cannibalistic nature of modern continental weathering and erosion: Earth and Planetary Science Letters, v. 401, p. 359-372.

Dellinger, M., Gaillardet, J., Bouchez, J., Calmels, D., Louvat, P., Dosseto, A., Gorge, C., Alanoca, L., Maurice, L., 2015, Riverine Li isotope fractionation in the Amazon River basin controlled by the weathering regimes: Geochimica et Cosmochimica Acta, v. 164, p. 71-93.

Dellinger, M., Bouchez, J., Gaillardet, J., Faure, L., Moureau, J., 2017, Tracing weathering regimes using the lithium isotope composition of detrital sediments: Geology, v. 45, p. 411-414.

Druhan, J. L., Steefel, C. I., Williams, K. H., DePaolo, D. J., 2013, Calcium isotope fractionation in groundwater: Molecular scale processes influencing field scale behavior: Geochimica et Cosmochimica Acta, v. 119, p. 93-116.

Druhan, J. L., & Maher, K., 2017, The influence of mixing on stable isotope ratios in porous media: A revised Rayleigh model: Water Resources Research, v. 53(2), p. 1101-1124.

Evans, M. J., Derry, L. A., Anderson, S. P., France-Lanord, C., 2001, Hydrothermal source of radiogenic Sr to Himalayan rivers: Geology, v. 29(9), p. 803-806.

Ferrier, K. L., Kirchner, J. W., 2008, Effects of physical erosion on chemical denudation rates: A numerical modeling study of soil-mantled hillslopes: Earth and Planetary Science Letters, v. 272, p. 591-599.

Flesch, G. D., Anderson Jr., A. R., Svec, H. J., 1973, A secondary isotopic standard for $^{6}Li/^{7}Li$ determinations: International Journal of Mass Spectrometry Ion Physics, v. 12(3), p. 2655-272.

Gibbs, R. J., 1967, The geochemistry of the Amazon River system: Part I. The factors that control the salinity and the composition and concentration of the suspended solids: Geological Society of America Bulletin, v. 78, p. 1203-1232.

Godfrey, L., Álvarez-Amado, F., 2020, Volcanic and saline lithium inputs to the Salar de Atacam: Minerals, v. 10, pp. 17.

Golla, J. K., Kuessner, M. L., Henehan, M. J., Bouchez, J., Rempe, D. M., & Druhan, J. L., 2021, The evolution of lithium isotope signatures in fluids draining actively weathering hillslopes: Earth and Planetary Science Letters, v. 567, p. 116988.

Gu, X., Rempe, D. M., Dietrich, W. E., West, A. J., Lin, T.-C., Jin, L., Brantley, S. L., 2020, Chemical reactions, porosity, and microfracturing in shale during weathering: The effect of erosion rate: Geochimica et Cosmochimica Acta, v. 269, p. 63-100.

Heidari, P., Li, L., Jin, L., Williams, J. Z., Brantley, S. L., 2017, A reactive transport model for Marcellus shale weathering: Geochimica et Cosmochimica Acta, v. 217, p. 421-440.

Hindshaw, R. S., Tosca, R., Goût, T. L., Farnan, I., Tosca, N. J., Tipper, E. T., 2019, Experimental constraints on Li isotope fractionation during clay formation. Geochimica et Cosmochimica Acta, v. 250, p. 219-237.

Holland H., 1984, The chemical evolution of the atmosphere and oceans: Princeton University Press.

Huh, Y., Chan, L.-H., Edmond, J. M., 2001, Lithium isotopes as a probe of weathering processes: Orinoco River: Earth and Planetary Science Letters, v. 194, p. 189-199.

Irion, G., 1983, Clay mineralogy of the suspended load of the Amazon and of rivers in the Papua-New Guinea mainland: Mitteilungen Geologie und Palaontolgie Institut Unversitat Hamburg, v. 55, p. 483-504.

Jasechko, S., Kirchner, J. W., Welker, J. M., McDonnell, J. J., 2016, Substantial proportion of global streamflow less than three months old: Nature Geoscience, v. 9, p. 126-129.

Jin, L., Ravella, R., Ketchum, B., Bierman, P. R., Heaney, P., White, T., Brantley, S. L., 2010, Mineral weathering and elemental transport during hillslope evolution at the Susquehanna/Shale Hills Critical Zone Observatory: Geochimica et Cosmochimica Acta, v. 74(13), p. 3669-3691.

Jung, H. and Navarre-Sitchler, A., 2018, Physical heterogeneity control on effective mineral dissolution rates: Geochimica et Cosmochimica Acta, v. 227, p. 246-263.

Kirchner, J.W., 2016, Aggregation in environmental systems – Part 1: Seasonal tracer cycles quantify young water fractions, but not mean transit times, in spatially heterogeneous catchments: Hydrology and Earth System Sciences, v. 20, p. 279-297.

Lara, M.C., Buss, H., Henehan, M.J., Schuessler, J.A., McDowell, W.H., 2022, Secondary minerals drive extreme lithium isotope fractionation during tropical weathering: JGR Earth Surface, v. 127, e2021JF006366.

Lasaga, A.C., 1998, Kinetic theory in the earth sciences: v. 811. Princeton, NJ: Princeton university press, 1998.

Lebedeva, M. I., Fletcher, R. C., Brantley, S. L., 2010, A mathematical model for steady-state regolith production at constant erosion rate: Earth Surface Processes and Landforms, v. 35, p. 508-524.

Lebedeva, M. I. and Brantley, S. L., 2013, Exploring geochemical controls on weathering and erosion of convex hillslopes: beyond the empirical regolith production function: Earth Surface Processes and Landforms, v. 38(15), p. 1793-1807.

Lechler, M., Pogge von Strandmann, P. A. E., Jenkyns, H. C., Prosser, G., Parente, M., 2015, Lithium-isotope evidence for enhanced silicate weathering during OAE 1a ,Early Aptian Selli event: Earth and Planetary Science Letters, v. 432, p. 210-222.

Lemarchand, E., Chabaux, R., Vigier, N., Millot, R., Pierret, M.-C., 2010, Lithium isotope systematics in a forested granitic catchment, Strengbach, Vosges Mountains, France: Geochimica et Cosmochimica Acta, v. 74(16), p. 4612-4628.

Li, G. and West, J. A., 2014, Evolution of Cenozoic seawater lithium isotopes: Coupling of global denudation regime and shifting seawater sinks: Earth and Planetary Science Letters, v. 401, p. 284-293.

Lowson, R. T., Comarmond, M.-C. J., Rajaratnam, G., Brown, P. L., 2005, The kinetics of the dissolution of chlorite as a function of pH and at 25°C: Geochimica et Cosmochimica Acta, v. 69(7), p. 1687-1699.

Maffre, P., Godderis, Y., Vigier, N., Moquet, J.-S., Carretier, S., 2020, Modelling the riverine δ^7Li variability throughout the Amazon Basin: Chemical Geology, v. 532, 119336.

Maher, K., Steefel, C. I., DePaolo, D. J., & Viani, B. E., 2006, The mineral dissolution rate conundrum: Insights from reactive transport modeling of U isotopes and pore fluid chemistry in marine sediments: Geochimica et Cosmochimica Acta, v. 70(2), p. 337-363.

Maher, K., 2010, The dependence of chemical weathering rates on fluid residence time: Earth and Planetary Science Letters, v. 294, p. 101-110.

Maher, K., 2011, The role of fluid residence time and topographic scales in determining chemical fluxes from landscapes: Earth and Planetary Sciences, v. 312, p. 48-58.

Maher, K., Chamberlain, C. P., 2014, Hydrologic regulation of chemical weathering and the geologic carbon cycle: Science, v. 343, p. 1502-1504.

Maher, K., von Blanckenburg, F., 2016, Surface ages and weathering rates from ^{10}Be ,meteoric, and ^{10}Be/^{9}Be: Insights from differential mass balance and reactive transport modeling: Chemical Geology, v. 446, p. 70-86.

Manaka, T., Araoka, D., Yoshimura, T., Hossain, H. M. Z., Nishio, Y., Suzuki, A., Kawahata, H., 2017, Downstream and seasonal changes of lithium isotope ratios in the Ganges-Brahmaputra river system: Geochemistry, Geophysics, Geosystems, v. 18(8), p. 3003-3015.

Maxwell, R. M., Condon, L. E., Kollet, S. J., Maher, K., Haggerty, R., Forrester, M. M., 2015, The imprint of climate and geology on the residence times of groundwater: Geophysical Research Letters, v. 43(2), p. 701-708.

Millot, R., Girard, J. P., 2007, Lithium isotope fractionation during adsorption onto mineral surfaces: Clay in Natural and Engineered Barriers for Radioactive Waste Confinement, 3rd International Meeting – Lille.

Millot, R., Negrel, P., 2007, Multi-isotopic tracing ,δ^{7}Li, δ^{11}B, ^{87}Sr/^{86}Sr, and chemical geothermometry: evidence from hydro-geothermal systems in France: Chemical Geology, v. 244, p. 664-678.

Millot, R., Negrel, P., Petelet-Giraud, E., 2007, Multi-isotopic Li, B, Sr, Nd, approach for geothermal reservoir characterization in the Limagne Basin, Massif Central, France: Applied Geochemistry, v. 22, p. 2307-2335.

Millot, R., Vigier, N., Gaillardet, J., 2010a, Behavior of lithium and its isotopes during weathering in the Mackenzie Basin, Canada: Geochimica et Cosmochimica Acta, v. 74, p. 3897-3912.

Millot, R., Scaillet, B., Sanjuan, B., 2010b, Lithium isotopes in arc geothermal systems: Guadeloupe, Martinique, French West Indies, and experimental approach: Geochimica et Cosmochimica Acta, v. 74, p. 1852-1871.

Millot, R., Hegan, A., Negrel P., 2012, Geothermal waters from the Taupo Volcanic Zone, New Zealand: Li, B, and Sr isotopes characterization: Applications in Geochemistry, v. 27, p. 677-688.

Misra, S., Froelich, P. N., 2012, Lithium isotope history of Cenozoic seawater: changes in silicate weathering and reverse weathering: Science, v. 335, p. 818-823.

Murphy, S. F., Brantley, S. L., Blum, A. E., White, A. F., Dong, H., 1998, Chemical weathering in a tropical watershed, Luquillo Mountains, Puerto Rico: II. Rate and mechanism of biotite weathering: Geochimica et Cosmochimica Acta, v. 62(2), p. 227-243.

Palandri, J. L. and Kharaka, Y. K., 2004, A compilation of rate parameters of water–mineral interaction kinetics for application to geochemical modeling Rep. 2004–1068: US Geological Survey Open File Report.

Pandey, S. and Rajaram, H., 2016, Modeling the influence of preferential flow on the spatial variability and time-dependence of mineral weathering rates: Water Resources Research, v. 52(12), p. 9344-9366.

Penniston-Dorland, S., Liu, X.-M., Rudnick, R. L., 2017, Lithium Isotope Geochemistry: Reviews in Mineralogy and Geochemistry, v. 82, p. 165-217.

Pistiner, J. S., and Henderson, G. M., 2003, Lithium-isotope fractionation during continental weathering process: Earth and Planetary Science Letters, v. 214, n. 1–2, p. 327–339.

Pogge von Strandmann, P. A. E., Henderson, G. M., 2015, The Li isotope response to mountain uplift: Geology, v. 43, p. 67-70.

Pogge von Strandmann, P. A. E., Jenkyns, H. C., Woodfine, R. G., 2013, Lithium isotope evidence for enhanced weathering during Oceanic Anoxic Event 2: Nature Geoscience, v. 6, p. 668-672.

Pogge von Strandmann, P. A. E, Burton, K. W., Opfergelt, S., Eiriksdottir, E. S., Murphy, M. J., Einarsson, A., Gislason, S. R., 2016, The effect of hydrothermal spring weathering processes and primary productivity on lithium isotopes: Lake Myvatn, Iceland: Chemical Geology, v. 445, p. 4-13.

Pogge von Strandmann, P. A. E., Desrochers, A., Murphy, M. J., Finlay, A. J., Selby, D., Lenton, T. M., 2017, Global climate stabilisation by chemical weathering during the Hirnantian glaciation: Geochemical Perspectives Letters, v. 3, p. 230-237.

Pogge von Strandmann, P. A. E., Kasemann, S. A., Wimpenny, J. B., 2020, Lithium and lithium isotopes in Earth's surface cycles: Elements, v. 16(4), p. 253-258.

Proust, D., Eymery, J.-P., Beaufort, D., 1986, Supergene vermiculitization of a magnesian chlorite: Iron and magnesium removal processes: Clays and Clay Minerals, v. 34, p. 572-580.

Steefel, C. I., C. A. J. Appelo, B. Arora, D. Jacques, T. Kalbacher, O. Kolditz, V. Lagneau, P. C. Lichtner, K. U. Mayer, J. C. L. Meeussen, S. Molins, D. Moulton, H. Shao, J. Simunek, N. Spycher, S. B. Yabusaki and G. T. Yeh, 2015, Reactive transport codes for subsurface environmental simulation: Computational Geosciences, v. 19(3), p. 445-478.

Sullivan, P. L., Hynek, S. A., Gu, X., Singha, K., White, T., West, N., Kim, H., Clarke, B., Kirby, E., Duffy, C., Brantley, S. L., 2016, Oxidative dissolution under the channel leads geomorphological evolution at the Shale Hills catchment: American Journal of Science, v. 316, p. 981-1026.

Sun, H., Xiao, Y., Gao, Y., Zhang, G., Casey, J. F., Shen, Y., 2018, Rapid enhancement of chemical weathering recorded by extremely light seawater lithium isotopes at the Permian-Triassic boundary: Proceedings of the National Academy of Sciences, v. 115(15), p. 3782-3787.

Tardy, Y., Krempp, G., Trauth, N., 1972, Le lithium dans les minéraux argileux des sédiments et des sols: Geochmica et Cosmochimica Acta, v. 36, p. 397-412.

Templeton, A. S., Chamberlain, C. P., Koons, P. O., and Craw, D., 1998, Stable isotopic evidence for mixing between metamorphic fluids and surface-derived waters during recent uplift of the Southern Alps, New Zealand: Earth and Planetary Science Letters, v. 154, p. 73-92.

Teng, F. Z., McDonough, W. F., Rudnick, R. L., Dalpe, C., Tomascak, P. B., Chappell, B. W., Gao, S., 2004, Lithium isotopic composition and concentration of the upper continental crust: Geochimica et Cosmochimica Acta, v. 68, p. 4167-4178.

Tomascak, P. B., 2004, Developments in the understanding and application of lithium isotopes in the earth and planetary sciences in geochemistry of non-traditional stable isotopes: Reviews in Mineralogy and Geochemistry, v. 55, p. 153-195.

Verney-Carron, A., Vigier, N., Millot, R., Hardarson, B. S., 2015, Lithium isotopes in hydrothermally altered basalts from Hengill, SW Iceland: Earth and Planetary Science Letters, v. 411, p. 62-71.

Vigier, N., Decarreau, A., Millot, R., Carignan, J., Petit, S., France-Lanord, C., 2008, Quantifying Li isotope fractionation during smectite formation and implications for the Li cycle: Geochimica et Cosmochimica Acta, v. 72, p. 780-792.

Vigier, N., Gislason, S., Burton, K., Millot, R., Mokadem, F., 2009, The relationship between riverine lithium isotope composition and silicate weathering rates in Iceland: Earth and Planetary Science Letters, v. 287, p. 434-441.

Wang, Y., Xu, H., 2001, Prediction of trace metal partitioning between minerals and aqueous solutions: a linear free energy correlation approach: Geochimica et Cosmochimica Acta, v. 65, p. 1529-1543.

Wanner, C., Sonnenthal, E. L., Liu, X.-M., 2014, Seawater δ^7Li: A direct proxy for global CO_2 consumption by continental silicate weathering?: Chemical Geology, v. 381, p. 154-167.

Williams, L. B., Hervig, R. L., 2005, Lithium and boron isotopes in illite-smectite: the importance of crystal size: Geochimica et Cosmochimica Acta, v. 24, p. 5705-5716.

Wimpenny J., Gisalason, S. R., James, R. H., Gannoun, A., Pogge von Strandmann, P. A. E., Burton, K. W., 2010, The behavior of Li and Mg isotopes during primary phase dissolution and secondary mineral formation in basalt: Geochimica et Cosmochimica Acta, v. 74, 5259-5279.

Winnick, M. J., Maher, K., 2018, Relationships between CO_2, thermodynamic limits on silicate weathering, and the strength of the silicate weathering feedback: Earth and Planetary Science Letters, v. 485, p. 111-120.

Wolery, T. J., Jackson, K. J., Bourcier, W. L., Bruton, C. J., Viani, B. E., Knauss, K. G., Delany, J. M., 1990, Current status of the EQ3/6 software package for geochemical modeling: ACS Symposium Series, v. 416, p. 104–116.

Zhang, L., Chan, L. H., Gieskes, J. M., 1998, Lithium isotope geochemistry of pore waters from Ocean Drilling Program Sites 918 and 919, Irminger Basin: Geochimica et Cosmochimica Acta v. 62, p. 2437-2450.

Zhang, X., Saldi, G. D., Schott, J., Bouchez, J., Kuessner, M, Montouillout, V., Henehan, M., Gailardet, J., 2021, Experimental constraints on Li isotope fractionation during the interaction between kaolinite and seawater. Geochimica et Cosmochimica Acta v. 292, p. 333-347.

Zhu, C., 2005, In situ feldspar dissolution rates in an aquifer: Geochimica et Cosmochimica Acta, v. 69(6), p. 1435-1453.

FIGURE CAPTIONS

Table 1. CrunchFlow Reaction Network.

Table 2. Weathering simulation scenarios.

Table 3. Variables calculated from model output.

Fig. 1. Conceptual diagram of lithium isotope systematics based on observational and theoretical studies (Bouchez and others, 2013; Dellinger and others, 2015). The top graph shows general patterns of δ^7Li_{diss} as a function of weathering intensity (WI), soil residence time, and dissolved Li concentrations. Points A, B, and C represent medium, high, and low WI, respectively, and are described in the Introduction. The bottom panel shows relative rates of regolith production, physical erosion (E), and chemical weathering (W), with increasing WI (left to right), along with depictions of idealized regolith profiles showing the weathering of primary minerals (gray) and accumulation of secondary minerals (brown).

Fig. 2. Batch reactor (Scenario 1) results for granitic weathering (no chlorite) showing the temporal evolution of (a) plagioclase and halloysite dissolution/precipitation rates; (b) weathering incongruence calculated as the ratio of halloysite precipitation to plagioclase dissolution rates; (c) dissolved Ca^{2+} concentration representing fully congruent weathering; and (d) dissolved Li^{+} concentrations across a range of partitioning coefficients (colored lines).

Fig. 3. Lithium isotope behavior in batch reactor experiments. (A) Temporal evolution of δ^7Li_{diss} for a range of partition coefficients (as in Fig. 2D); (B) δ^7Li_{diss} as a function of fraction Li left in

solution. Amazon basin data from Dellinger and others (2015) shown in gray, and samples interpreted to reflect floodplain uptake processes denoted.

Fig. 4. No Erosion (Scenario 2) CrunchFlow simulations of weathering profiles showing (a) plagioclase solid phase (vol. %); (b) halloysite solid phase (vol. %); (c) weathering incongruence (ratio of instantaneous halloysite precipitation to plagioclase dissolution rates); (d) dissolved $[Ca^{2+}]$, (e) dissolved $[Li^{+}]$, and (d) $\delta^{7}Li_{diss}$. Simulation timesteps are denoted by line color. Simulations depicted have a P_{Li} value of 0.9.

Fig. 5. Crunchflow simulations of granitic weathering (Scenario 3) including uplift and erosion. Weathering profile results for low (a-e), medium (f-j), and high (k-o) weathering intensity conditions. Columns from left to right show solid phase plagioclase, solid phase halloysite, weathering incongruence, dissolved $[Li^{+}]$, and $\delta^{7}Li_{diss}$. Gray shading denotes un-weathered bedrock defined as model cells with <101% initial porosity. Colored lines denote model timestep. Red bars in d, i, and n denote approximate observational ranges of $[Li^{+}]$ from Dellinger and others (2015) for low, medium, and high weathering intensity, respectively. Simulations depicted have a P_{Li} value of 0.9.

Fig. 6. Crunchflow simulations including chlorite (Scenario 4) and vermiculite minerals from Table 1. Weathering profile results for low (a-d), medium (e-h), and high (i-l) weathering intensity conditions. Columns from left to right show solid phase plagioclase, solid phase chlorite, dissolved $[Li^{+}]$, and $\delta^{7}Li_{diss}$. Gray shading denotes un-weathered bedrock defined as model cells with <101% initial porosity. Colored lines denote model timestep. Red bars in c, g, and k denote approximate observational ranges of $[Li^{+}]$ from Dellinger and others (2015) for low, medium, and high weathering intensity, respectively. Simulations depicted have a P_{Li} value of 0.9.

Fig. 7. Relationships between $\delta^{7}Li_{diss}$ and Weathering Intensity (left) and dissolved Li concentrations (right). Results show model output (a-b) without chlorite; (c-d) with chlorite; and (e-f) global riverine observations from Dellinger and others (2015) and references therein. Simulations depicted have a P_{Li} value of 0.9.

Fig. 8. $\delta^{7}Li$ of fine-grained suspended material as a function of weathering intensity for CrunchFlow simulations (black dots; no chlorite simulations) and observational data from the Amazon basin (Dellinger and others, 2017). Model output includes the full range of lithium partition coefficients shown in Figure 3, and CrunchFlow output range is denoted by gray shading.

APPENDIX FIGURE CAPTIONS

Table A1. CrunchFlow reaction network for plagioclase dissolution – beidellite precipitation batch reactor sensitivity experiments.

Fig. A1. Relationships between $\delta^{7}Li_{diss}$ and Weathering Intensity (left) and dissolved Li concentrations (right) for erosion/uplift simulations with chlorite across a range of P_{Li} values.

Fig. A2. Batch reactor output for plagioclase dissolution and beidellite precipitation showing (left) mineral precipitation/dissolution rates; (center) weathering congruence; and (right) δ^7Li_{diss} as a function of time for a range of P_{Li} values.

Fig. B1. Changes in Li concentrations and δ^7Li_{diss} with mean fluid transit time assuming a gamma-function transit time distribution with alpha value of 1. The discharge arrow shows qualitative relationships between discharge and mean transit times and demonstrating negative C-Q relationships for Li concentrations and δ^7Li_{diss} in simulations.

Table 1. CrunchFlow reaction network.

Mineral	Reaction	log(K_{eq}) @ 298 K	log(k)
Plagioclase (An_{20})	$Ca_{0.2}Na_{0.79739}{}^{7}Li_{0.002409}{}^{6}Li_{0.0001948}Al_{1.2}Si_{2.8}O_8 \leftrightarrow 0.2Ca^{2+} + 0.79739Na^{+} + 0.002409{}^{7}Li^{+} + 0.0001948{}^{6}Li^{+} + 1.2AlO_2^{-} + 2.8SiO_2(aq)$	-20.076	-14.84
Quartz	$SiO_2(qz) \leftrightarrow SiO_2(aq)$	-3.9993	-55
Halloysite_^{7}Li	$Al_{2-0.33x}{}^{7}Li_xSi_2O_5(OH)_4 + 6H^{+} \leftrightarrow (2-0.33x)AlO_2^{-} + x{}^{7}Li^{+} + 2SiO_2(aq) + H_2O$ *	-36.4537	-17.14
Halloysite_^{6}Li	$Al_{2-0.33x}{}^{6}Li_xSi_2O_5(OH)_4 + 6H^{+} \leftrightarrow (2-0.33x)AlO_2^{-} + x{}^{6}Li^{+} + 2SiO_2(aq) + H_2O$ *	-36.4537	Precip: -17.13225 Diss: -17.14
Chlorite [a]	$Mg_{1.03969}{}^{7}Li_{0.0005769}{}^{6}Li_{0.00004683}Fe_{0.2}K_{1.28}Al_{2.24}Si_3H_{13.52}O_{18} + 10.48H^{+} \leftrightarrow 1.03989Mg^{2+} + 0.0005769{}^{7}Li^{+} + 0.00004683{}^{6}Li^{+} + 0.2Fe^{2+} + 1.28K^{+} + 2.24Al^{3+} + 3SiO_2(aq) + 12H_2O$	14.996	-13
Vermiculite [a]	$Mg_{0.1997}{}^{7}Li_{0.000576923}{}^{6}Li_{0.00004683}Fe_{0.441}K_{1.3}Al_{4.4}Si_{1.6}H_{8.52}O_{15.2} + 15.5H^{+} \leftrightarrow 0.2Mg^{2+} + 0.010962{}^{7}Li^{+} + 0.0008897{}^{6}Li^{+} + 0.3941Fe^{2+} + 1.3K^{+} + 4.4Al^{3+} + 1.6SiO_2(aq) + 12H_2O$	-5.39	-13

* x varies from 0.00035 - 0.0043

[a] Based on Heidari et al. (2017)

Table 2. Weathering simulation scenarios

Weathering Scenarios	Simulation Length (kyrs)	Infiltration Rate (m/yr)	Uplift/Erosion Rate (mm/yr)	Weathering Intensity
Scenario 1. Batch Reactor	10	NA	NA	NA
Scenario 2. "Chronosequence"	1000	0.5	NA	NA
Scenario 3. Uplift/Erosion	500	0.01 - 5	0.005 - 0.2	0.00045 - 0.927
Scenario 4. Uplift/Erosion w/ Chlorite	500	0.01 - 5	0.005 - 0.2	0.0056 - 0.72

Table 3. Variables calculated from model output

Model Output/Metric	Formula	Description
Erosion Rate (Mass) (t/km^2/yr)	$E = RP*BD$	Prescribed volumentic regolith production (mm/yr) multiplied by bulk density (BD; kg/m^3) in the top model cell
Chemical Denudation Rate (t/km^2/yr)	$W = Q*([Ca^{2+}] + [Mg^{2+}] + [Na^{+}] + [K^{+}] + [SiO2_{(aq)}])*1000$	Prescribed infiltration rate (Q; m/yr) multiplied by dissolved solute load (g/L), evaluated at model domain base and weathering zone base
Weathering Intensity	$WI = W/(W + E)$	Ratio of chemical denudation rate to total denudation rate
Suspended Load δ^7Li (‰)	$\delta^7 Li_{sus} = (M_{plag}*C_{plag}*\delta^7 Li_{plag} + M_{chlor}*C_{chlor}*\delta^7 Li_{chlor} + M_{halloy}*C_{halloy}*\delta^7 Li_{halloy})/(M_{plag}*C_{plag} + M_{chlor}*C_{chlor} + M_{halloy}*C_{halloy})$	Lithium mass-weighted δ^7Li composition of non-quartz minerals in the eroding top model cell, where M represents mineral mass and C represents mineral lithium concentration
Weathering Incongruence	$I = -R_{halloysite}/R_{plagioclase}$	Instaneous ratio of halloysite precipitation to plagioclase dissolution rates

Figure 1

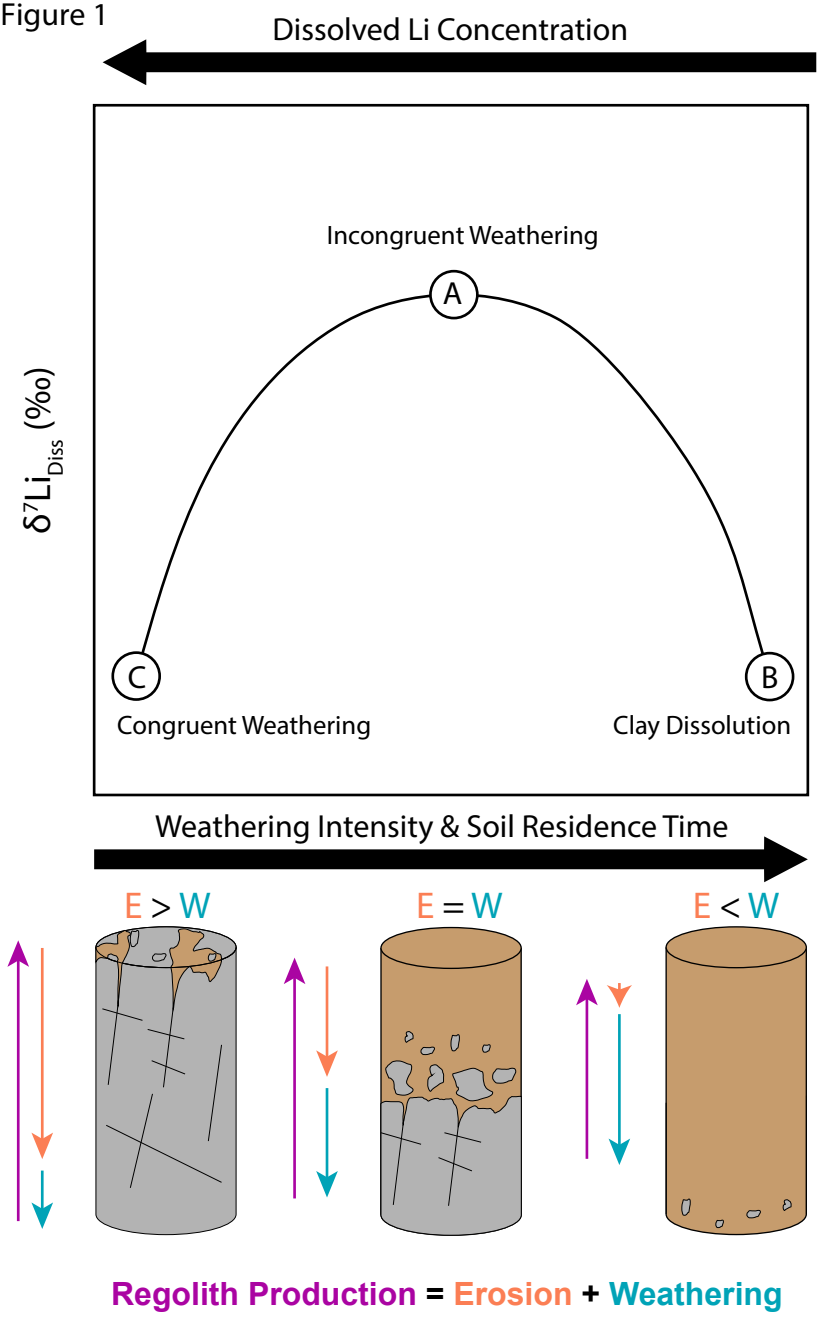
Dissolved Li Concentration
Incongruent Weathering
A
δ^7Li_{Diss} (‰)
C
Congruent Weathering
B
Clay Dissolution
Weathering Intensity & Soil Residence Time
E > W
E = W
E < W
Regolith Production = Erosion + Weathering

Figure 2

a)

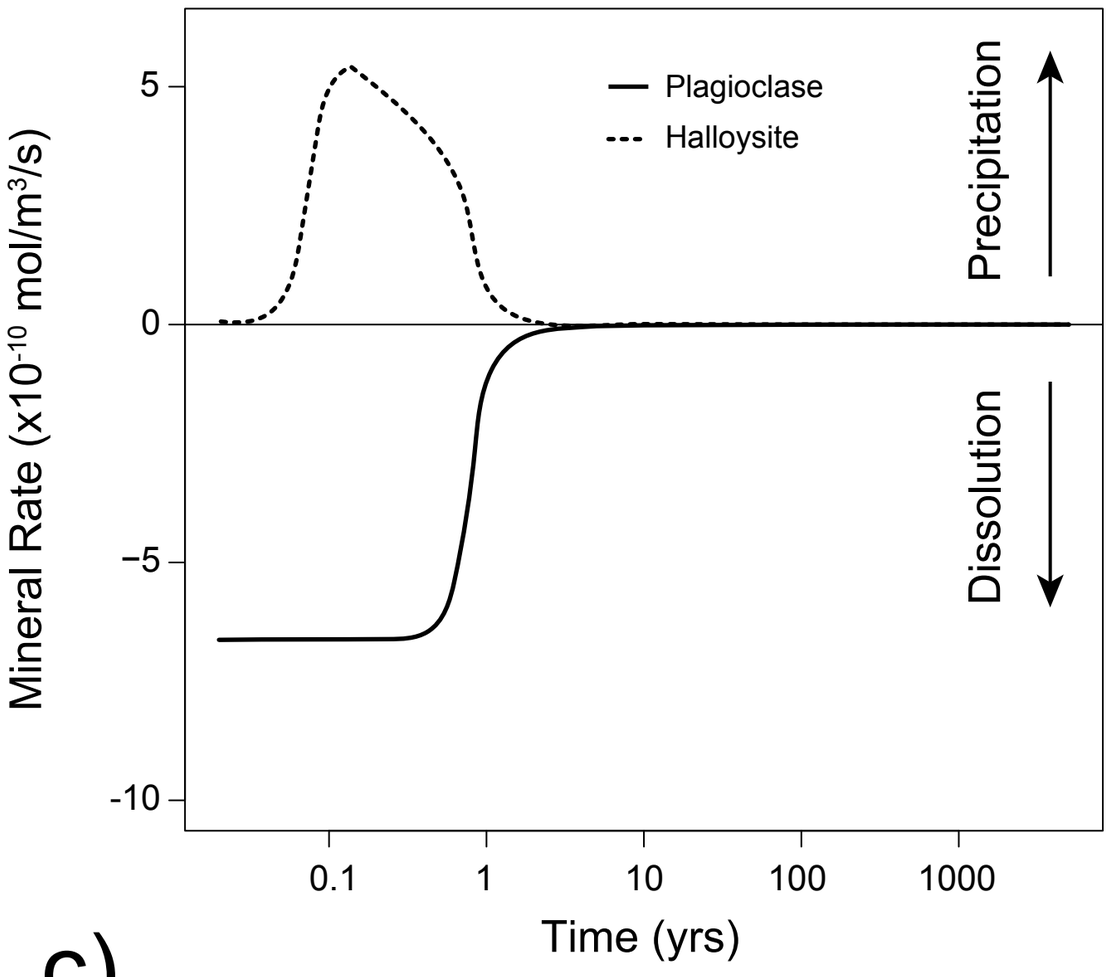

b)

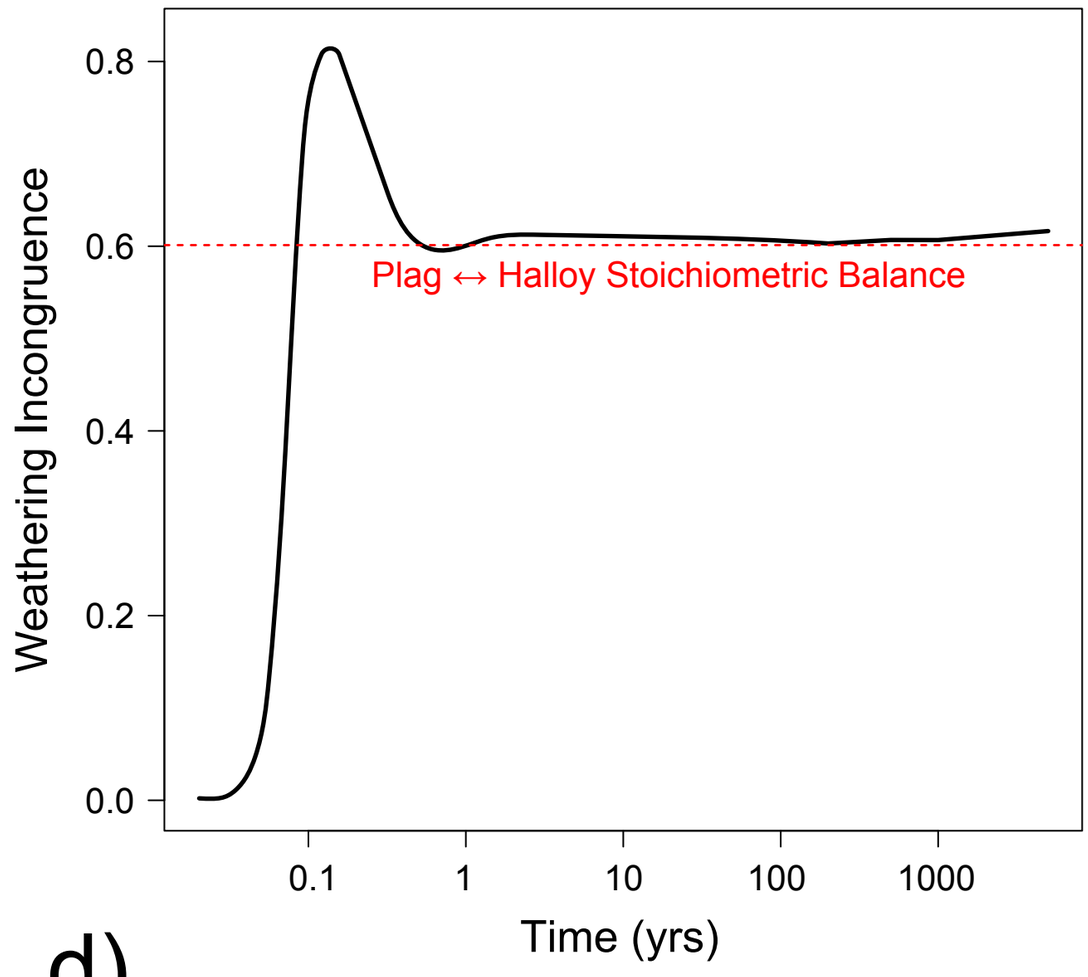

c)

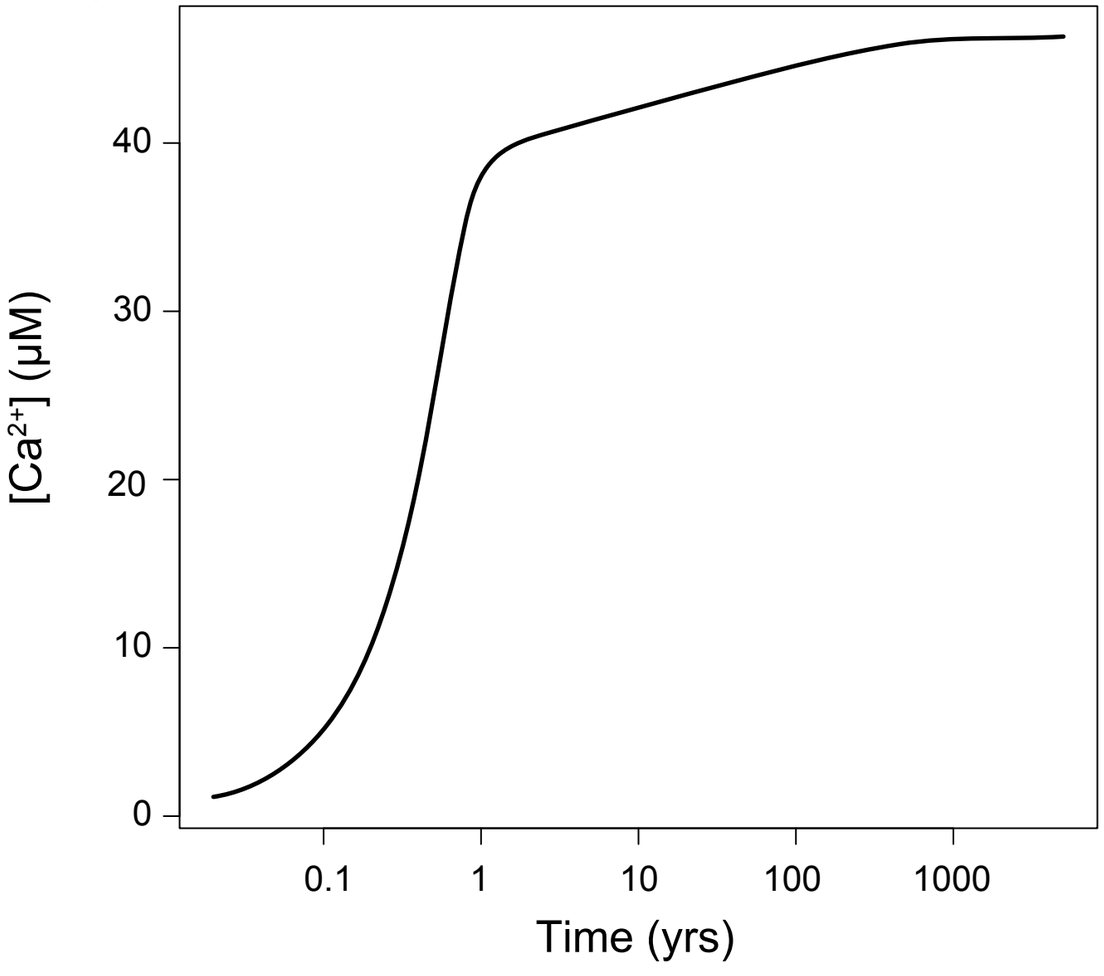

d)

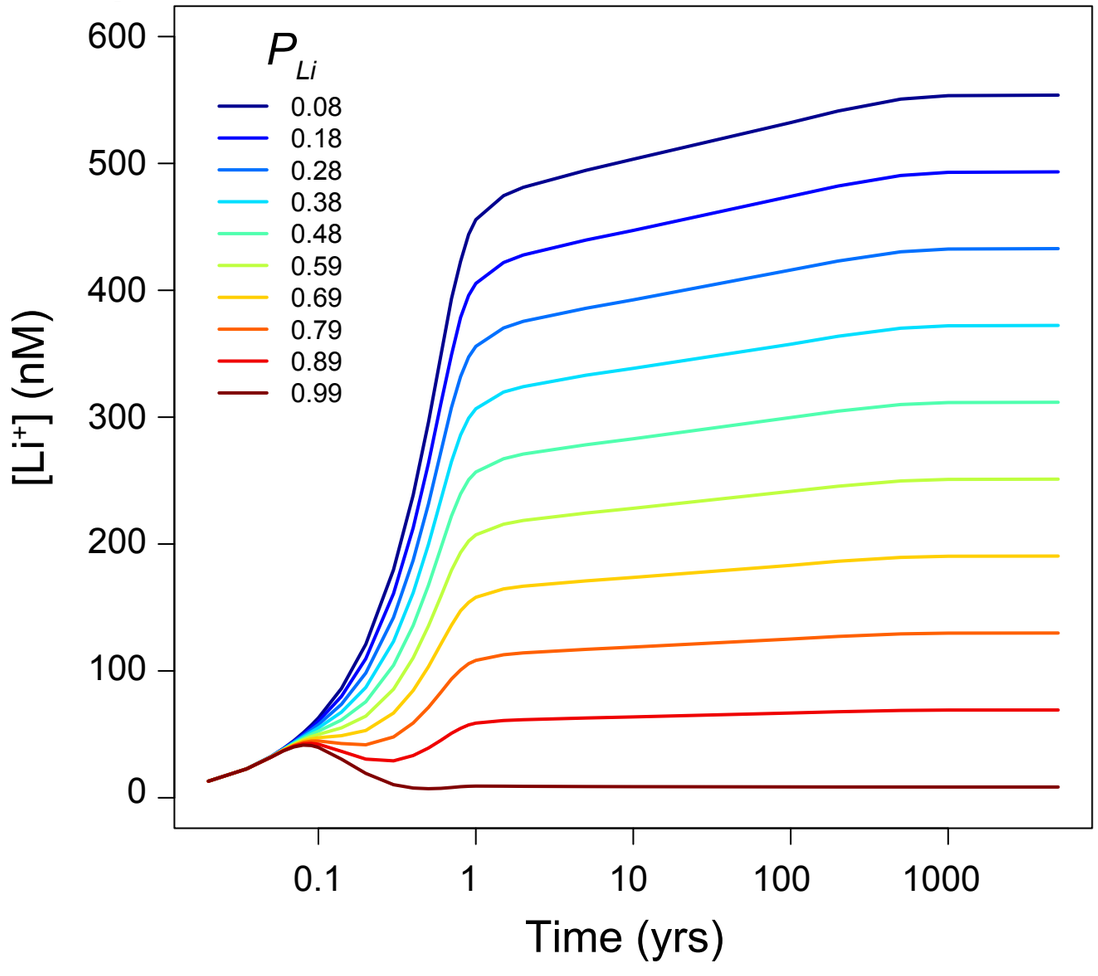

Figure 3

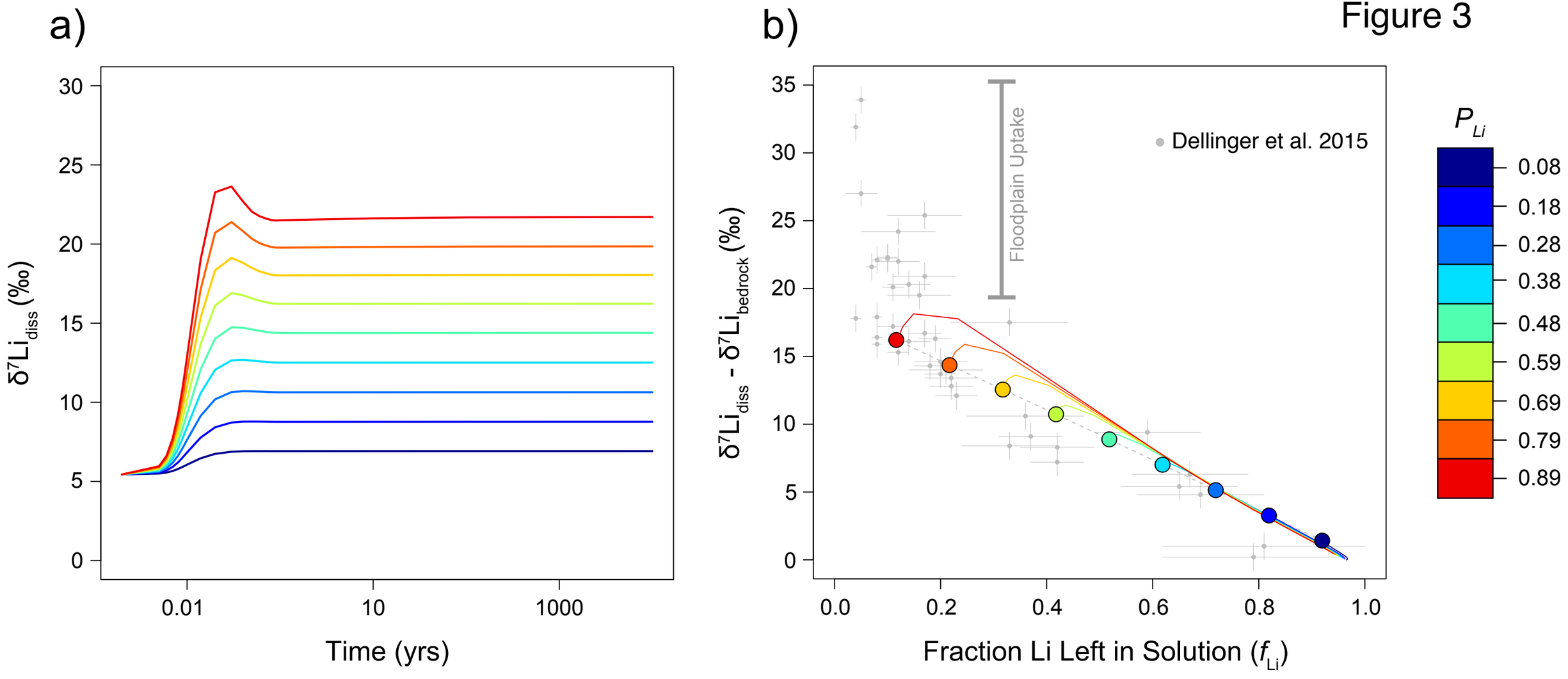
a)
b)
δ^7Li_{diss} (‰)
Time (yrs)
0.01
10
1000
δ^7Li_{diss} - $\delta^7Li_{bedrock}$ (‰)
Fraction Li Left in Solution (f_{Li})
Floodplain Uptake
Dellinger et al. 2015
P_{Li}
0.08
0.18
0.28
0.38
0.48
0.59
0.69
0.79
0.89

Figure 4

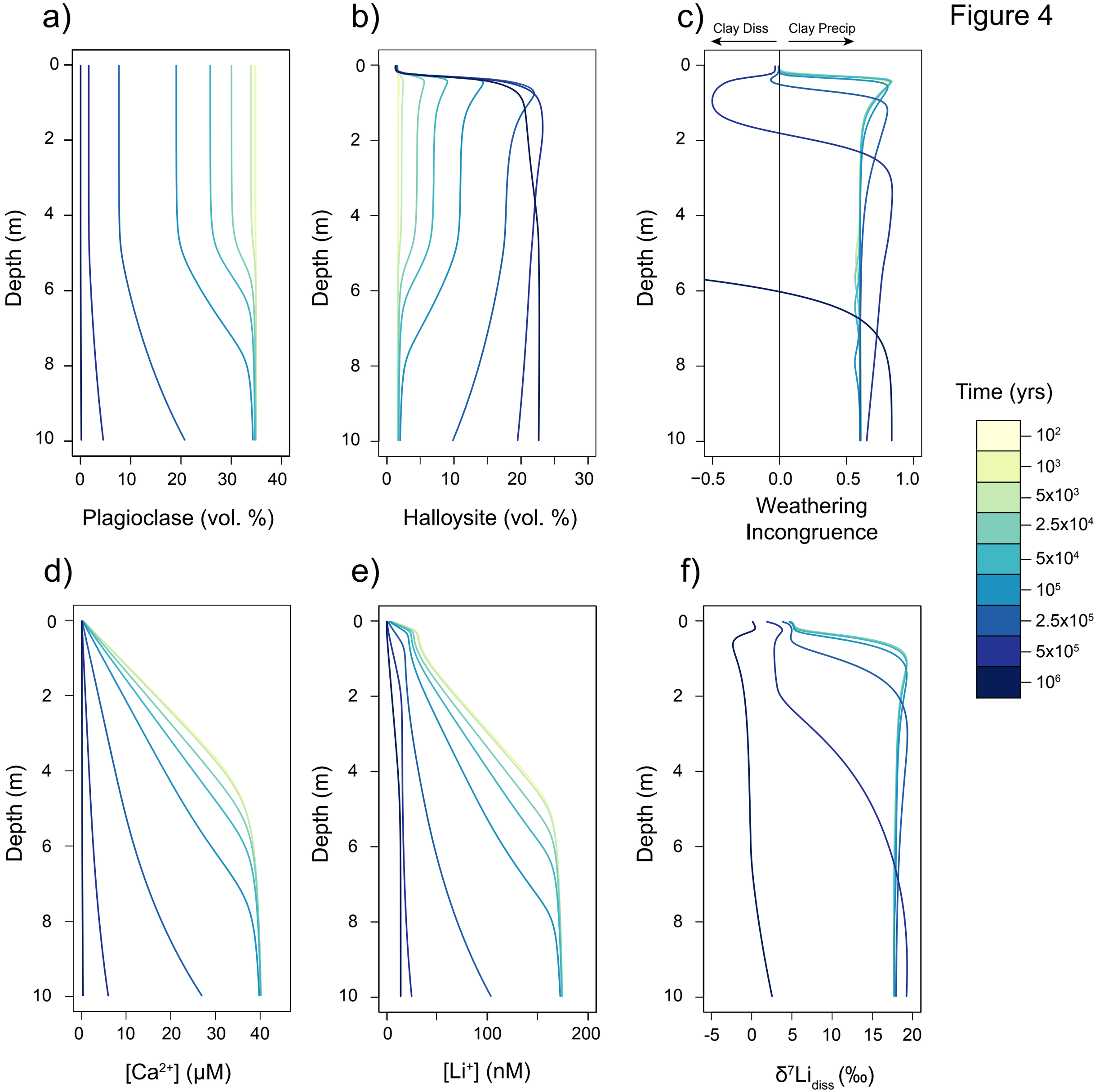
a)
b)
c)
Clay Diss
Clay Precip
Depth (m)
Plagioclase (vol. %)
Halloysite (vol. %)
Weathering Incongruence
Time (yrs)
10²
10³
5x10³
2.5x10⁴
5x10⁴
10⁵
2.5x10⁵
5x10⁵
10⁶
d)
e)
f)
[Ca²⁺] (μM)
[Li⁺] (nM)
δ⁷Li_diss (‰)

Figure 5

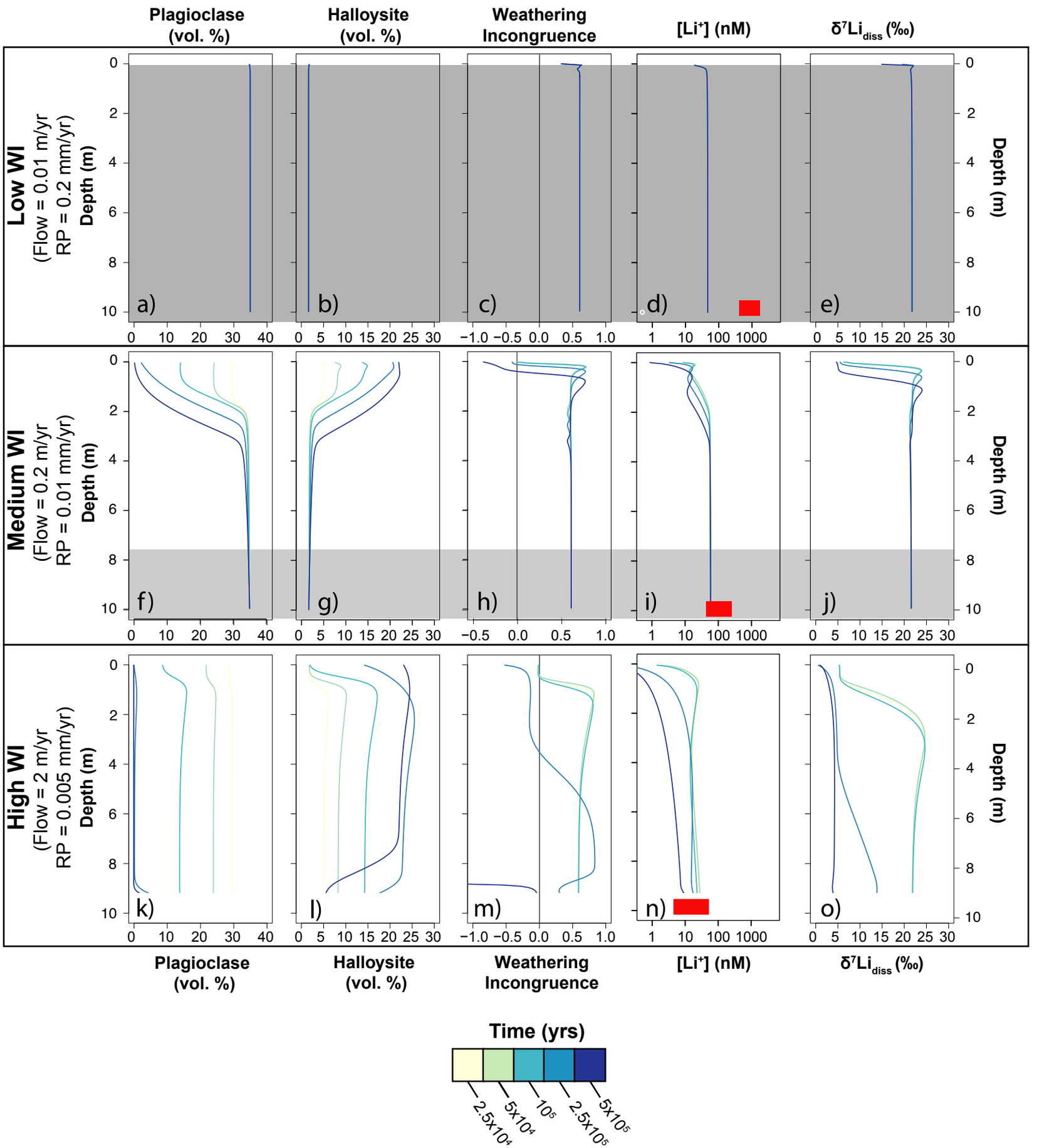
Plagioclase (vol. %)
Halloysite (vol. %)
Weathering Incongruence
[Li+] (nM)
δ7Lidiss (‰)
Low WI
(Flow = 0.01 m/yr
RP = 0.2 mm/yr)
Depth (m)
Medium WI
(Flow = 0.2 m/yr
RP = 0.01 mm/yr)
High WI
(Flow = 2 m/yr
RP = 0.005 mm/yr)
a)
b)
c)
d)
e)
f)
g)
h)
i)
j)
k)
l)
m)
n)
o)
Time (yrs)
2.5x10⁴
5x10⁴
10⁵
2.5x10⁵
5x10⁵

Figure 6

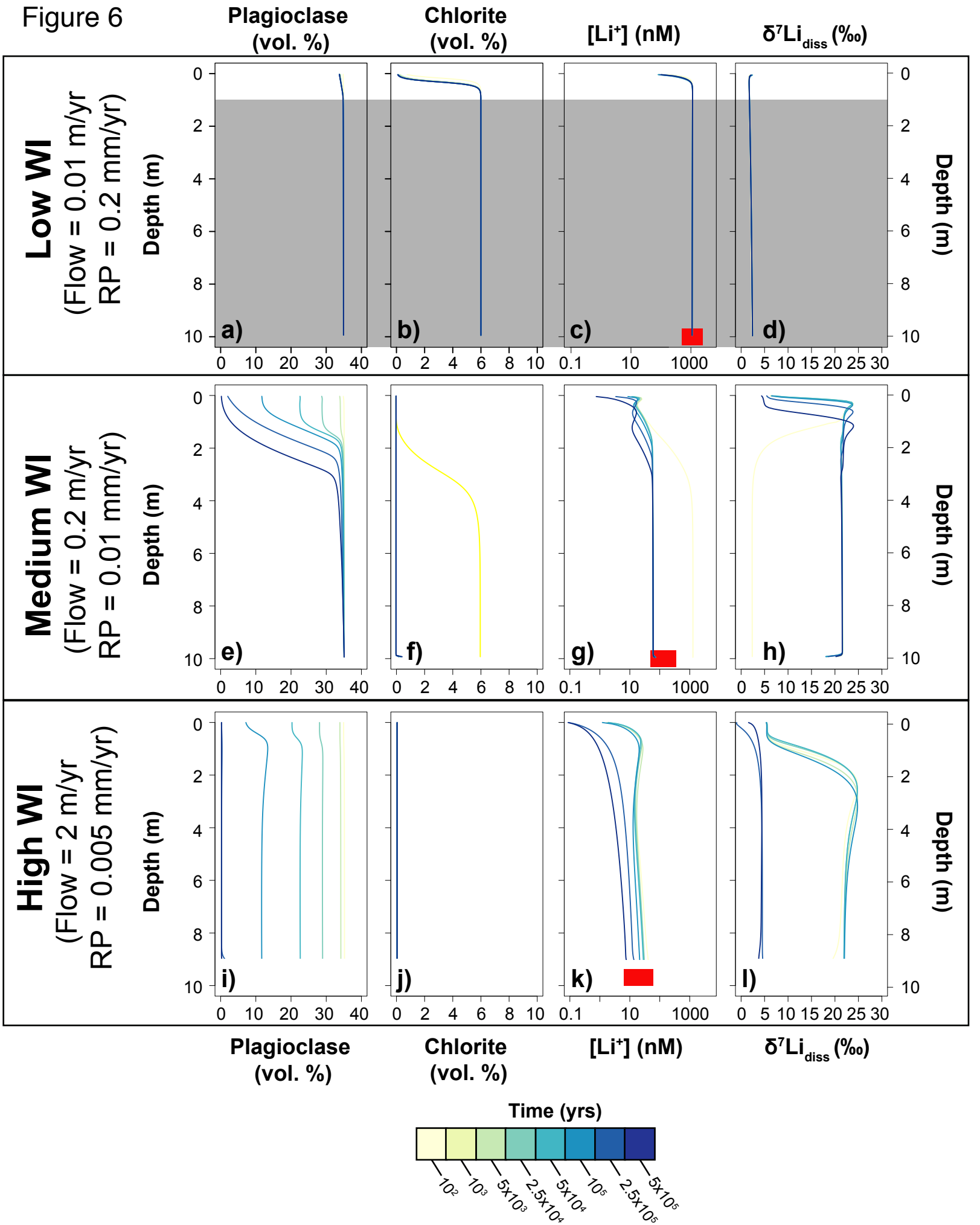
Plagioclase (vol. %)
Chlorite (vol. %)
[Li+] (nM)
δ7Lidiss (‰)
Low WI
(Flow = 0.01 m/yr
RP = 0.2 mm/yr)
Medium WI
(Flow = 0.2 m/yr
RP = 0.01 mm/yr)
High WI
(Flow = 2 m/yr
RP = 0.005 mm/yr)
Depth (m)
a)
b)
c)
d)
e)
f)
g)
h)
i)
j)
k)
l)
Time (yrs)
10²
10³
5x10³
2.5x10⁴
5x10⁴
10⁵
2.5x10⁵
5x10⁵

Figure 7

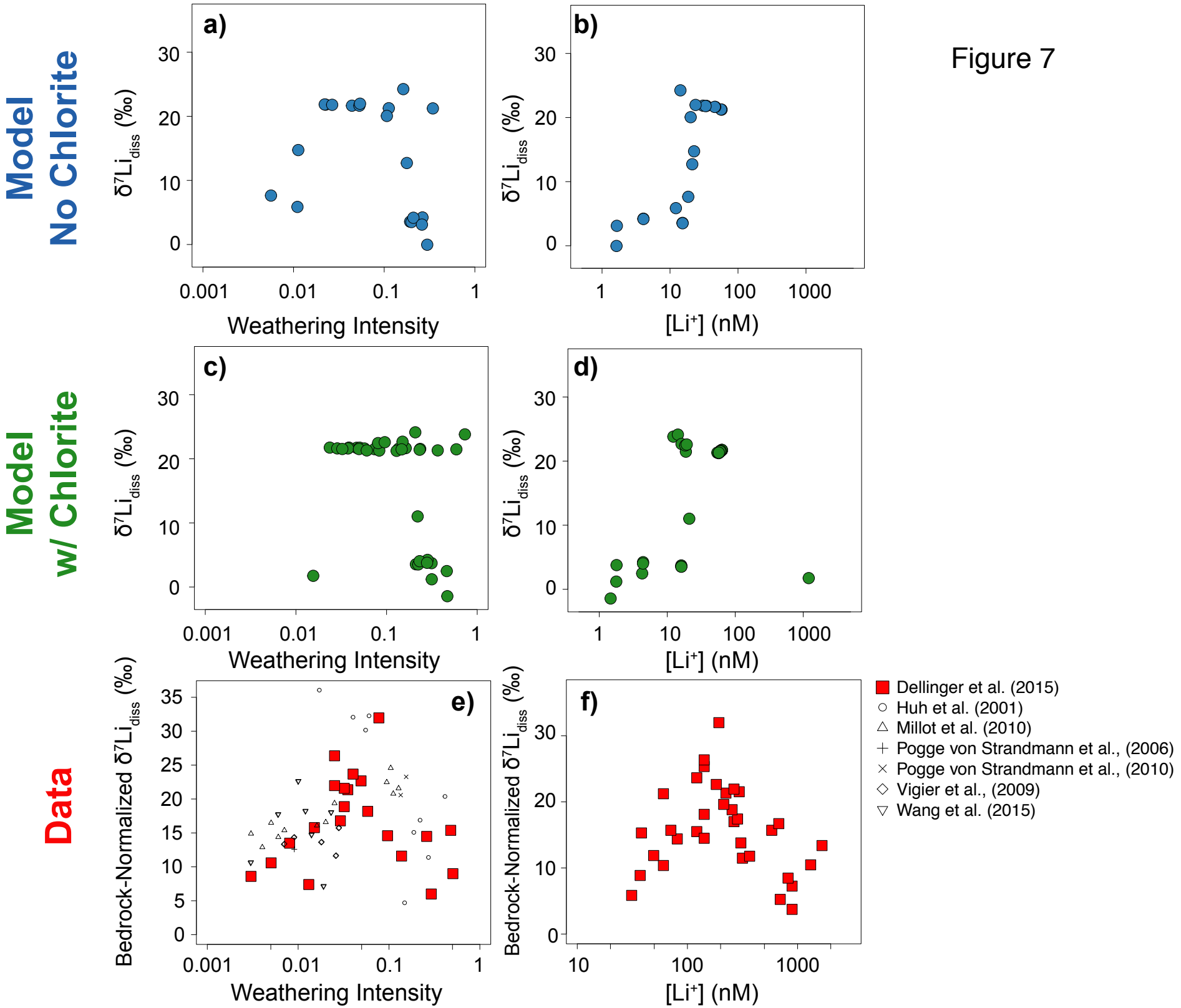
Model
No Chlorite
Model
w/ Chlorite
Data
a)
b)
c)
d)
e)
f)
δ^7Li_{diss} (‰)
Bedrock-Normalized δ^7Li_{diss} (‰)
Weathering Intensity
[Li+] (nM)
Dellinger et al. (2015)
Huh et al. (2001)
Millot et al. (2010)
Pogge von Strandmann et al., (2006)
Pogge von Strandmann et al., (2010)
Vigier et al., (2009)
Wang et al. (2015)

Figure 8

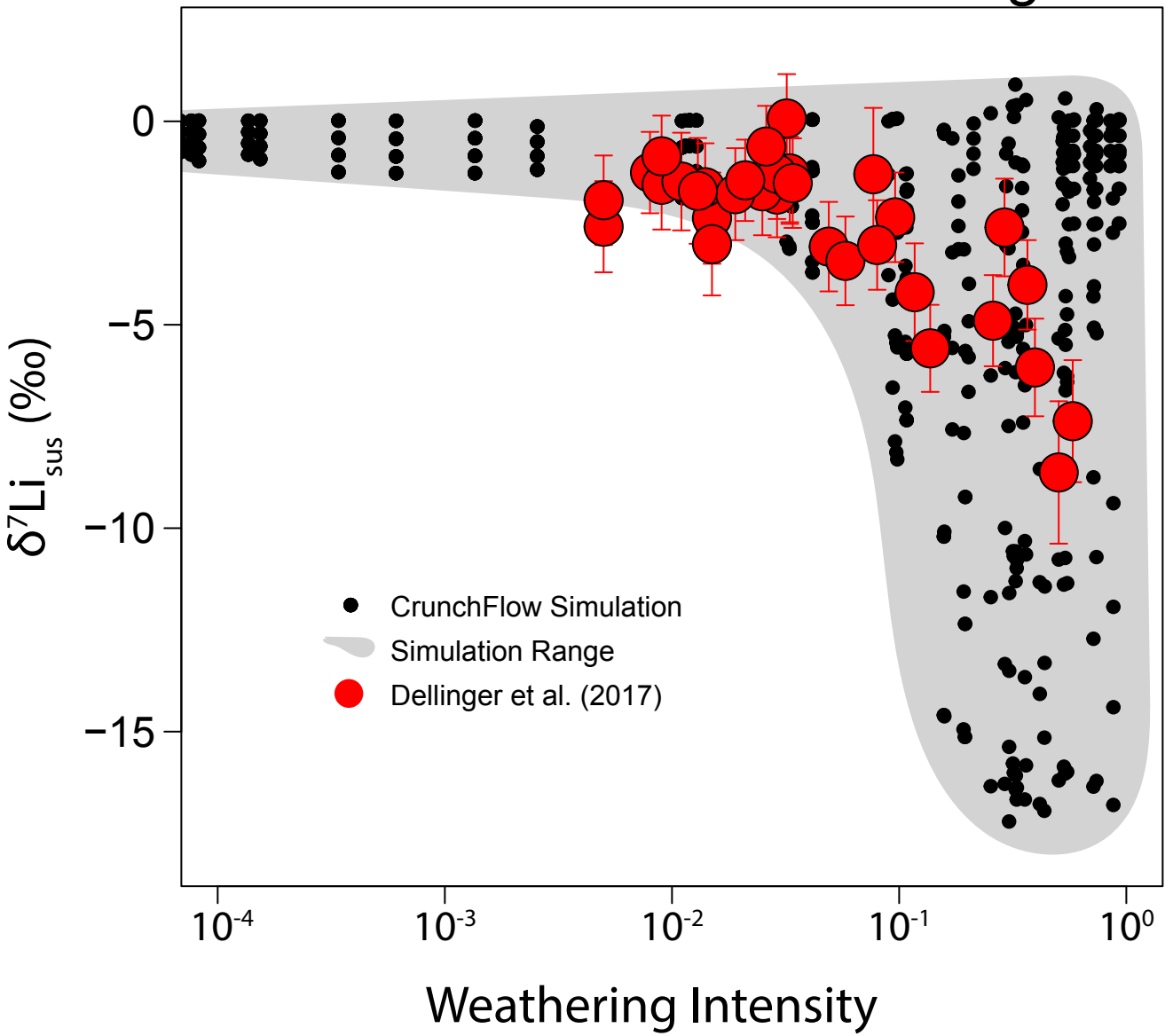
0
−5
−10
−15
δ^7Li_{sus} (‰)
CrunchFlow Simulation
Simulation Range
Dellinger et al. (2017)
10^{-4}
10^{-3}
10^{-2}
10^{-1}
10^{0}
Weathering Intensity

Table A1. CrunchFlow reaction network with 2:1 clay phase.

Mineral	Reaction	log(K_{eq}) @ 298 K	log(k)
Plagioclase (An_{20})	$Ca_{0.2}Na_{0.79739}{}^{7}Li_{0.002409}{}^{6}Li_{0.0001948}Al_{1.2}Si_{2.8}O_8 \leftrightarrow 0.2Ca^{2+} + 0.79739Na^{+} + 0.002409{}^{7}Li^{+} + 0.0001948{}^{6}Li^{+} + 1.2AlO_2^{-} + 2.8SiO_2(aq)$	-20.076	-14.84
Quartz	$SiO_2(qz) \leftrightarrow SiO_2(aq)$	-3.9993	-55
Ca-Beidellite_^{7}Li	$Ca_{0.165\text{-}0.5x}{}^{7}Li_xAl_{2.33}Si_{3.67}O_{10}(OH)_2 + 7.32H^{+} \leftrightarrow (0.165\text{-}0.5x)Ca^{2+} + 2.33Al^{3+} + x{}^{7}Li^{+} + 3.67SiO_2(aq) + 4.66H_2O$ *	5.59	-17.14
Ca-Beidellite_^{6}Li	$Ca_{0.165\text{-}0.5x}{}^{6}Li_xAl_{2.33}Si_{3.67}O_{10}(OH)_2 + 7.32H^{+} \leftrightarrow (0.165\text{-}0.5x)Ca^{2+} + 2.33Al^{3+} + x{}^{6}Li^{+} + 3.67SiO_2(aq) + 4.66H_2O$ *	5.59	Precip: -17.13225 Diss: -17.14

* x varies from 0.000402 - 0.004945

Figure A1

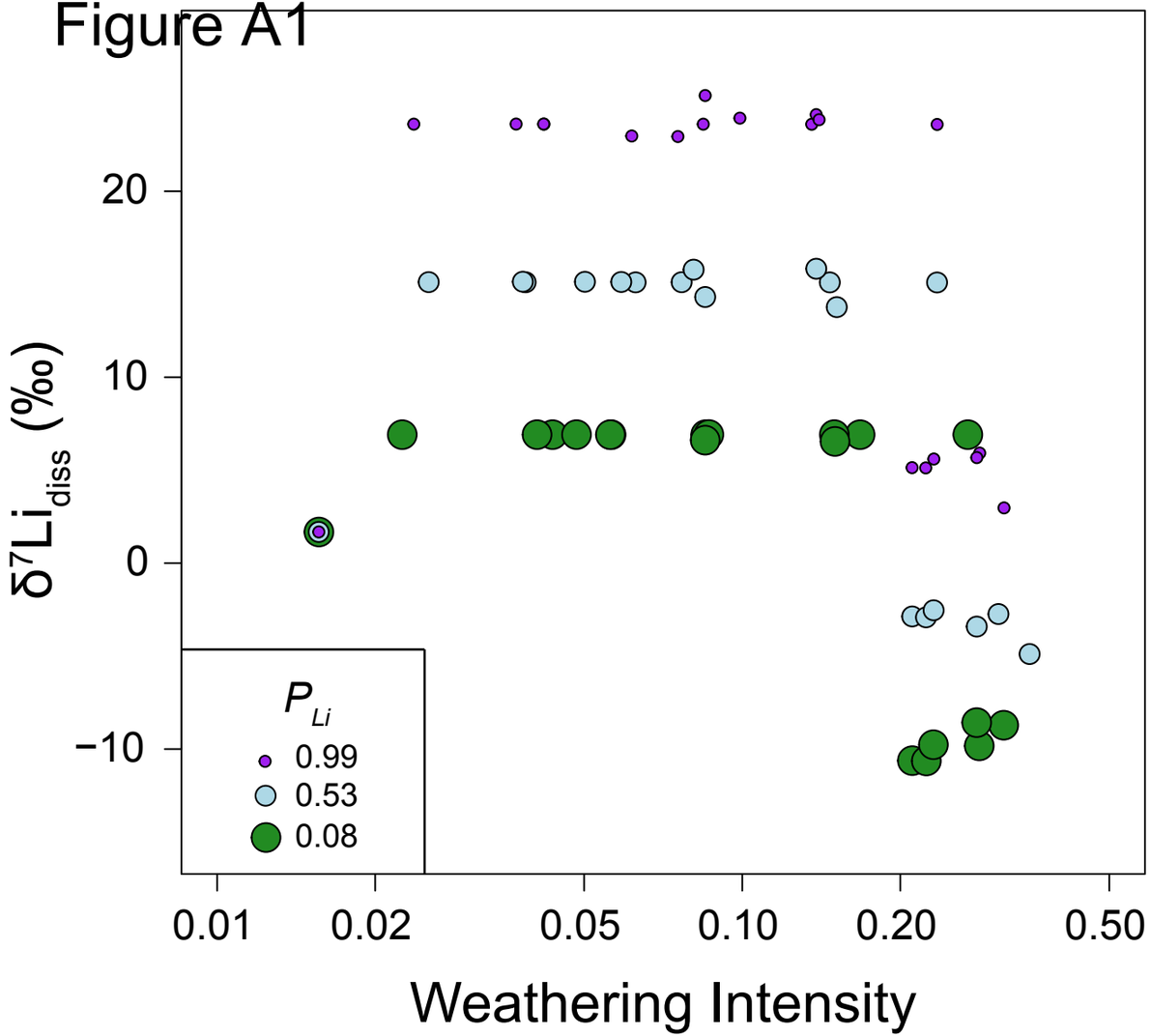
20
10
0
−10
δ^7Li_{diss} (‰)
P_{Li}
0.99
0.53
0.08
0.01
0.02
0.05
0.10
0.20
0.50
Weathering Intensity

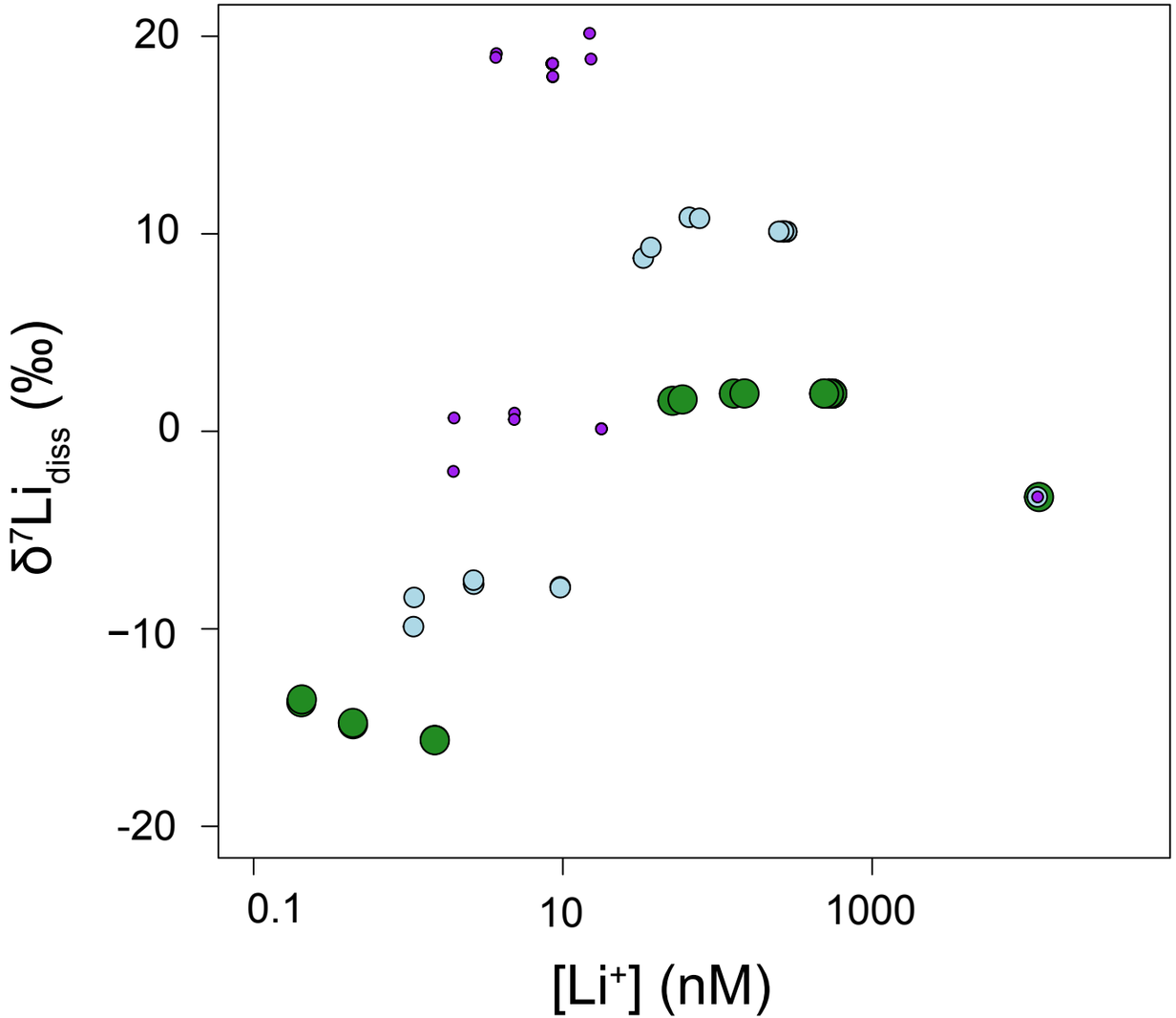
20
10
0
−10
-20
δ^7Li_{diss} (‰)
0.1
10
1000
[Li⁺] (nM)

Figure A2

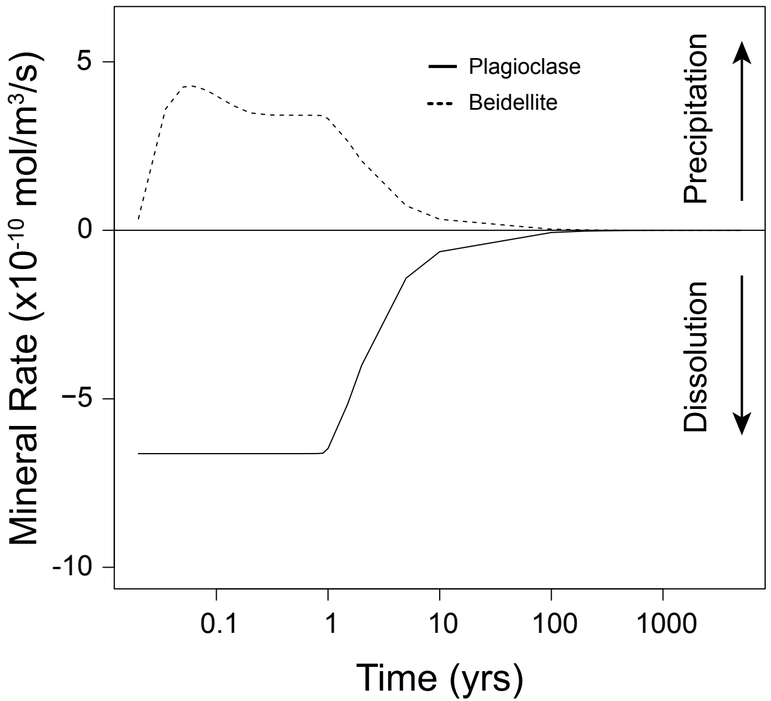
Plagioclase
Beidellite
Precipitation
Dissolution
Mineral Rate (x10^{-10} mol/m^3/s)
5
0
−5
-10
0.1
1
10
100
1000
Time (yrs)

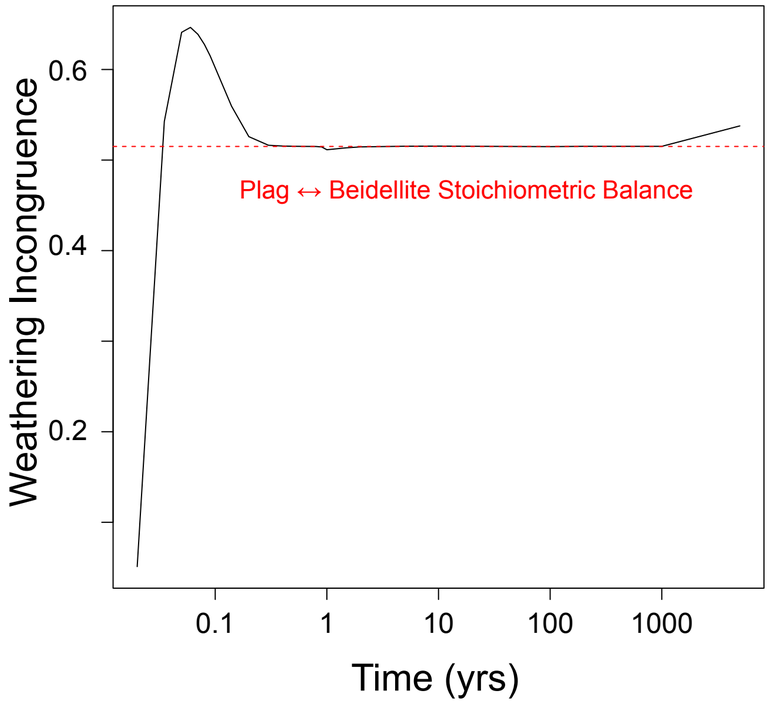
Plag ↔ Beidellite Stoichiometric Balance
Weathering Incongruence
0.6
0.4
0.2
0.1
1
10
100
1000
Time (yrs)

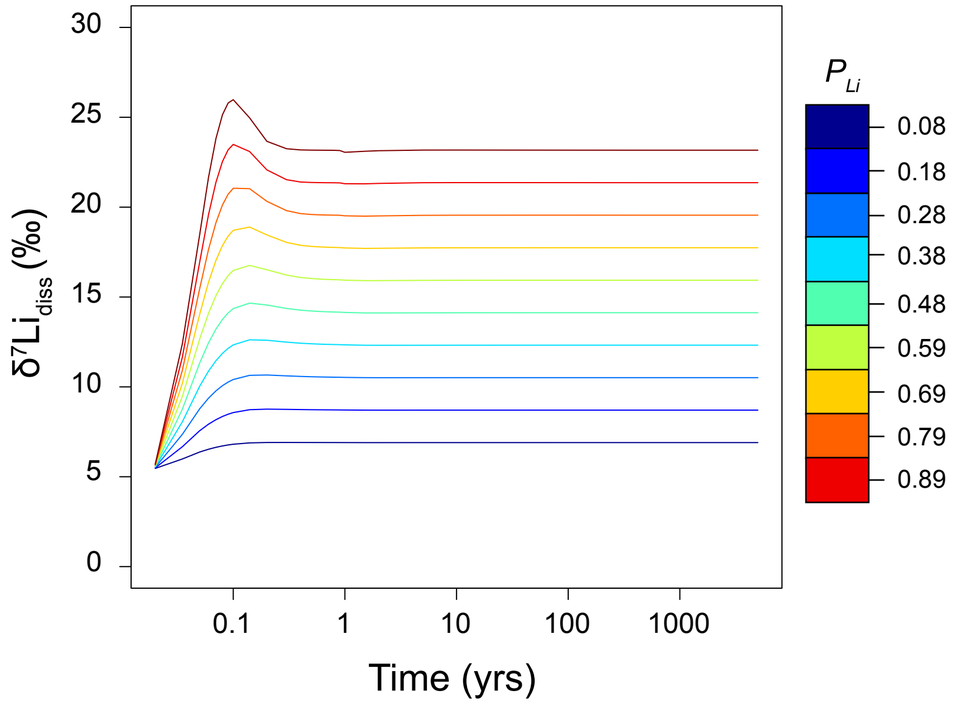
P_{Li}
0.08
0.18
0.28
0.38
0.48
0.59
0.69
0.79
0.89
δ^7Li_{diss} (‰)
30
25
20
15
10
5
0
0.1
1
10
100
1000
Time (yrs)

Figure B1

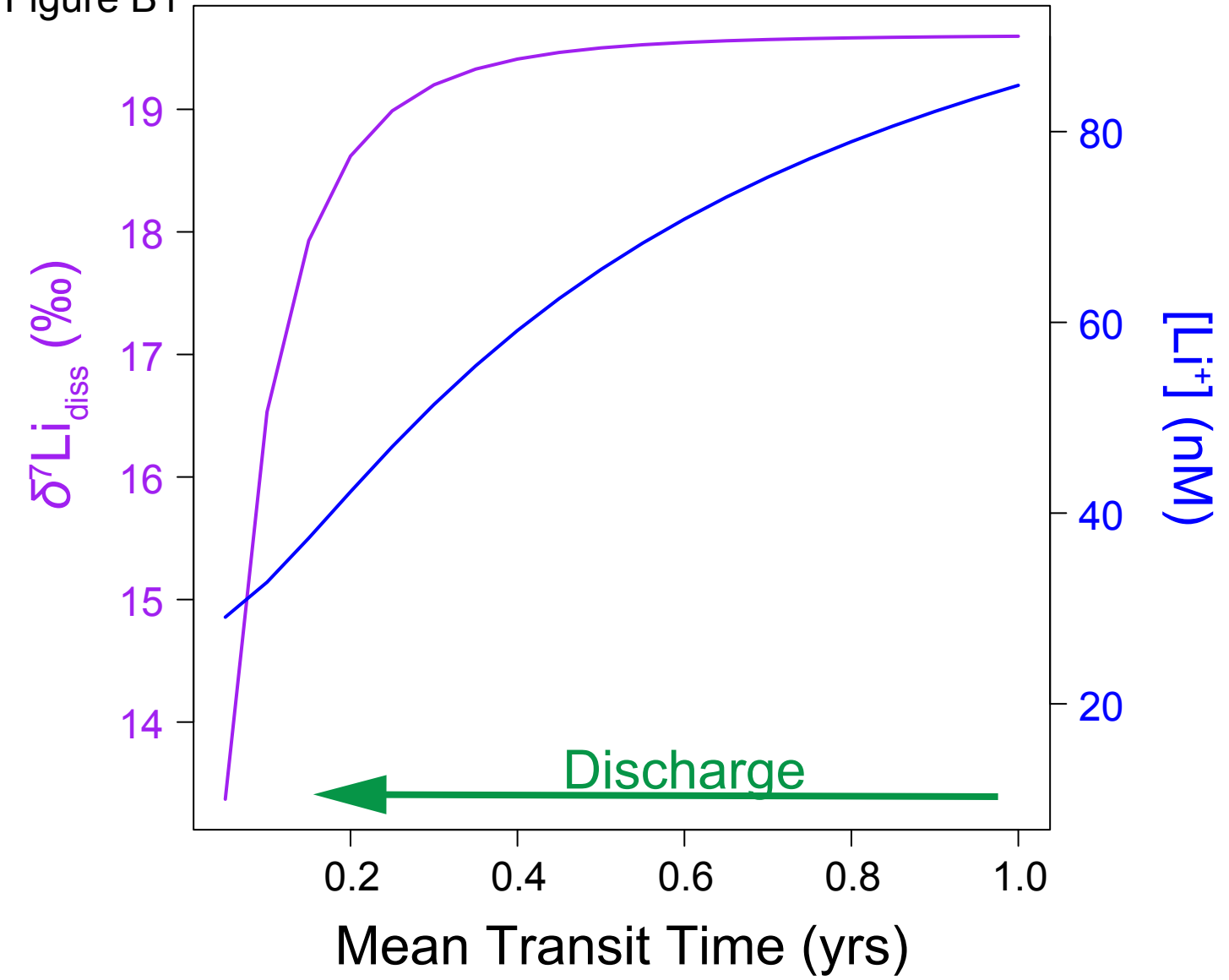
19
18
17
16
15
14
δ^7Li_{diss} (‰)
80
60
40
20
[Li+] (nM)
Discharge
0.2
0.4
0.6
0.8
1.0
Mean Transit Time (yrs)